High-spin States and K-isomers of ^{185}Re

Albert B. F. Lee

A thesis submitted for the degree of
Bachelor of Science with Honours in Physics of
The Australian National University

01 November, 2006

Declaration

This thesis is an account of research undertaken between February 2006 and October 2006 at The Department of Nuclear Physics, Research School of Physical Sciences and Engineering, The Australian National University, Canberra, Australia.

Except where acknowledged in the customary manner, the material presented in this thesis is, to the best of my knowledge, original and has not been submitted in whole or part for a degree in any university.

Albert B. F. Lee
01 November, 2006

Acknowledgements

First of all, I am very grateful to my dedicated supervisor, Greg Lane for providing me with constant help and support on my Honours project. I would also like to thank Justin Werner (MSc Student) who gave me advice on relative time spectra, and Hiroshi Watanabe (PostDoc) who taught me how to do angular correlations. Last but not least, thanks to my family and friends; my mother and brother, Henry, Andreas, Winston, Riyadh, Neil, Liam, Duncan and John for moral support throughout my Honours year. Without all of you, this thesis could not have been written.

Abstract

The structure of ^{185}Re was studied using inelastic excitation of an enricged ^{185}Re target with 820 MeV ^{136}Xe ions and the techniques of γ-ray spectroscopy. The known level scheme of ^{185}Re below the isomer at 2124 keV has been significantly extended. The 2124 keV long-lived isomer has been remeasured to have $T_{1/2} = 200 \pm 4$ ns, and four isomers below this state have been characterised and their half-lives measured as 26 ± 2 ns at 368 keV, 1.3±0.6 ns at 1207 keV and 5.5±1.4 ns at 1411 keV. Through a comprehensive angular correlation analysis and consideration of K-forbidden transition strengths, the spins and parities of all states up to the $T_{1/2} = 200$ ns isomer at 2124 keV have been firmly identified. Five multi-quasiparticle states were identified, with the following configurations proposed, $13/2^{-}\nu\{3/2^{-}[512], 1/2^{-}[510]\} \otimes \pi 9/2^{+}[514]$, $15/2^{-}\nu\{9/2^{+}[624], 1/2^{-}[510]\} \otimes \pi 5/2^{+}[402]$, $19/2^{-}\nu\{3/2^{-}[512], 11/2^{+}[615]\} \otimes \pi 5/2^{+}[402]$, $23/2^{-}\nu\{3/2^{-}[512], 11/2^{+}[615]\} \otimes \pi 5/2^{+}[402]$ and $25/2^{-}(\nu\{9/2^{+}[624], 11/2^{+}[615]\} \otimes \pi 5/2^{+}[402]$. A comparison of excitation energies with multi-quasiparticle calculations is required to reproduce the low excitation energies for some of the states.

Contents

List of Figures

List of Tables

Chapter 1

Introduction

Nuclei are made up of strongly interacting protons and neutrons that move in a potential generated by the sum of their own interactions. The nuclear shell model [1] describes the energy levels for protons and neutrons in an attractive central potential with strong spin-orbit coupling [2] as shown in equation 1.1:

$$V_{tot} = V_{cent} - V_{ls}\langle l.s\rangle \tag{1.1}$$

where V_{tot} is the total potential of the nucleus, V_{cent} is the attractive central potential dependent on the number of nucleons, and $V_{ls}\langle l.s\rangle$ is the potential due to the coupling between orbital angular momentum l, and spin, s. The energy levels calculated for nuclei with the potential described in equation 1.1 exhibit large energy gaps in the single particle spectrum , each corresponding to a *magic number* which represents the cumulative number of nucleons filling the levels. Nuclei in the region of *magic numbers* (with closed shells) are spherical in shape, however, away from closed shells, nuclei can be deformed and we extend to the deformed shell model, an example of which is the Nilsson model [3]. The Nilsson model considers that a nucleus can be deformed in two possible ways; prolate, where the nucleus is stretched like a rugby ball, and oblate, where the nucleus is compressed from opposite sides, which resembles the shape of the Earth [4]. In the Nilsson model, the nuclear energy levels are split because of the deformation. As a consequence, every state is charactericed by the projection, Ω of the angular momentum j $(1/2, 3/2, 5/2, \dots, j)$ on the symmetry axis of the nucleus (see Figure 1.1).

There are a total of $j + 1/2$ states associated with every spherical state with angular momentum j, resulting from the number of possible angular momentum projections on the symmetry axis. The maximum number of nucleons which can fill a spherical state is $2j+1$, so each of the different levels with a projection of Ω have a maximum occupancy of 2. For example, the $2d_{5/2}$ proton orbital splits into three different Nilsson states; $5/2^+[402]$, $3/2^+[411]$ and $1/2^+[420]$ in the prolate region (see Figure 1.2). These Nilsson states can be occupied up to 2 protons each, and in ^{185}Re, there is an odd proton which lies in the $5/2^+[402]$ state.

However, the split in the levels are more complex in reality, and an actual Nilsson diagram indicating the split for every spherical parent in the shell model for nuclei with 50 to 82 number of protons is shown in Figure 1.3.

A low-lying state in an odd-mass deformed nucleus is characterised by the occupancy of an odd nucleon in a Nilsson state, which describes the angular momentum projection of the odd nucleon on the symmetry axis, Ω. However, a pair in other Nilsson states which initially do not contribute to the total projection Ω, of the nucleus may be broken, and there would be two more odd nucleons in two other Nilsson states. The total projection

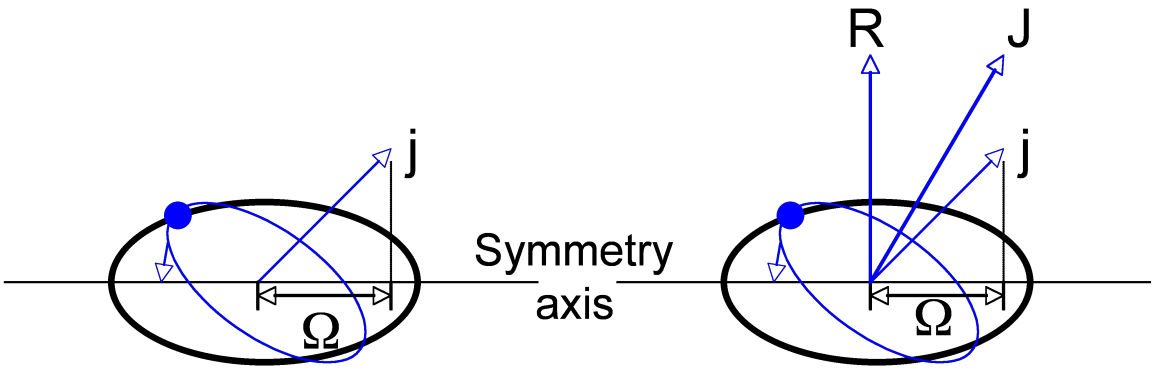

Figure 1.1: Left: A prolate-deformed nucleus with single-particle angular momentum j and symmetry axis projection Ω. Right: The same nucleus with an additional angular momentum R due to rotation. The resulting angular momentum for the nucleus is represented by J.

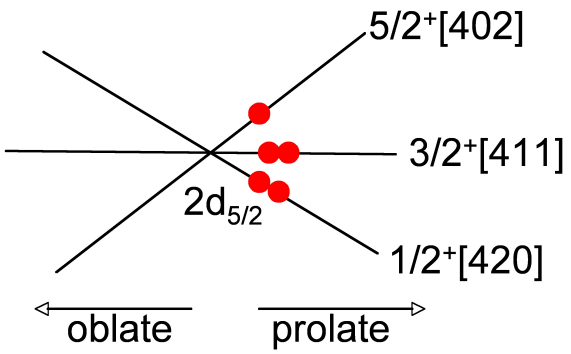

Figure 1.2: Splitting of the $2d_{5/2}$ orbital. The ground state of ^{185}Re is a single proton in the $5/2^+[402]$ Nilsson state.

of these three nucleons will add, resulting in a larger value of Ω for the nucleus. More complex situations could occur, where there are five odd nucleons in five different Nilsson states, or more. Although it is not discussed in detail here, in practice it is also necessary to allow for the effects of nuclear pairing and transform from the simple Nilsson single particle levels into quasiparticle levels.

A deformed system can also generate energy via rotation (See Figure 1.1) and therefore, for every intrinsic configuration with one or more odd nucleons in the Nilsson states, a rotational band can be built upon it. The rotational excited states in a nucleus are characterised by a quantum mechanical analogue of the classical rotor, with energies given by:

$$E_R = \frac{\hbar^2}{2\mathcal{I}} R(R+1) \tag{1.2}$$

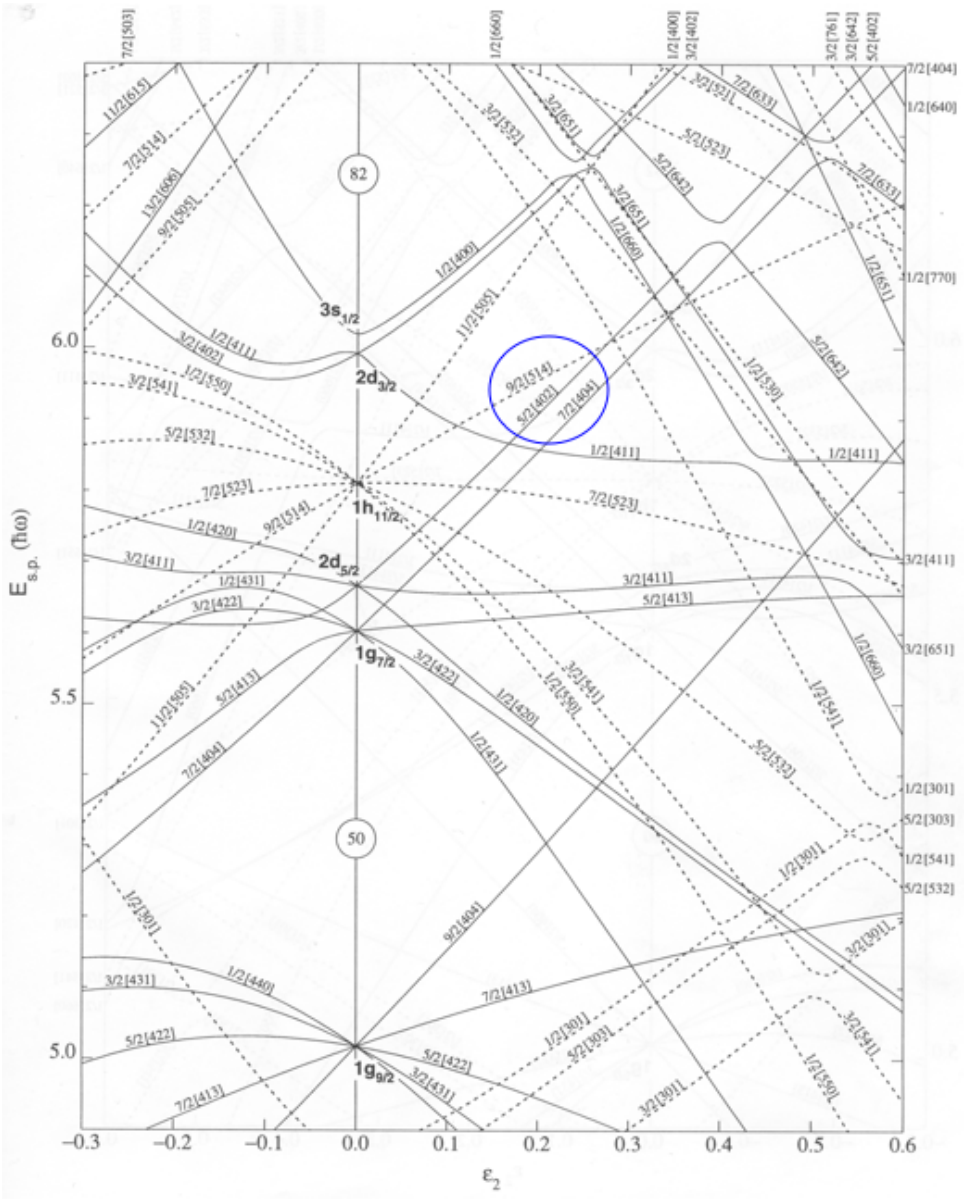

Figure 1.3: Nilsson diagram for protons, $50 \leq Z \leq 82$ where Z is the number of protons, $E_{s.p.}(\hbar\omega)$ is the single particle energy, and ϵ_2 is the deformation parameter. The ^{185}Re nucleus is prolate-deformed with $\epsilon_2 \sim 0.23$. The $9/2^-[514]$, $5/2^+[402]$ and the $7/2^+[404]$ states (in the circle) are the levels lying close to the proton Fermi surface for ^{185}Re.

The moment of inertia, $\mathcal{I}$ is related to the deformation of the nucleus, and R is the rotational spin of the excited states. For intrinsic states with non-zero total angular momentum, the spin separation between adjacent states, ΔJ in the rotational band is always equals to 1 [3, 5].

The detailed structure of nuclei is determined by the pattern of excited states from which can be identified, the various modes of excitation which include single-particle levels and rotational excitations. This thesis describes the results of an experiment which used the techniques of γ-ray spectroscopy to deduce the level scheme for ^{185}Re and understand its nuclear structure.

1.1 Electric and Magnetic Transitions

Nuclei have electric and magnetic fields due to the motion of the electric and magnetic moments of the constituent protons and neutrons [1]. When these fields change in a transition from one quantum state to another, the nucleus will emit electromagnetic radiation. These radiations can be characterised into electric (E) and magnetic (M) transitions with the multipolarity of a transition represented by XL, where X is either electric or magnetic, and L ($L = 1, 2, 3, \ldots, N$) is the multipole order of the transition. If there is a change in parity between the initial and final states, the possible transitions are even electric and odd magnetic, and if there is no change in parity, the opposite is true. While there are many different transition possibilities for a given spin and parity change, these transitions can never carry an angular momentum less than the difference in spin between the initial and final states, and no more than the sum of the initial and final spins [1] as shown below:

$$|J_i + J_f| \geq L \geq |J_i - J_f| \tag{1.3}$$

where J_i and J_f are the initial and final angular momentum of the nuclear states respectively. Furthermore, the probability of these transitions decreases with increasing multipole order(see Section 1.2), so very high multipolarity transitions are strongly hindered [8].

1.2 Transition Probability

The transition strengths for typical single-particle like transitions have been estimated theoretically by Weisskopf [6, 7], and they are characterised by the reduced transition probability, $B_w(XL)$:

For electric transitions;

$$B_w(EL) = \frac{(1.2)^{2L}}{4\pi}\left(\frac{3}{L+3}\right)^2 A^{2L/3} \tag{1.4}$$

For magnetic transitions;

$$B_w(ML) = \frac{10}{\pi}(1.2)^{2L-2}\left(\frac{3}{L+2}\right)^2 A^{(2L-2)/3} \tag{1.5}$$

where A is the mass number of the nucleus. The total probability of a transition out of a nuclear excited state can be determined from experimental measurement of its meanlife:

$$P(level) = \frac{1}{\tau(level)} \tag{1.6}$$

where P(level) is the total transition probability and τ(level) is the meanlife of the excited state. To compare experimental values with theoretical predictions, another parameter called the partial γ-ray transition probability, $P_\gamma(XL)$ is required. It is obtained from the total transition probability by [8]:

$$P_\gamma(XL) = P(level)\frac{I_\gamma}{\Sigma_T I_T} \tag{1.7}$$

where I_γ is the γ-ray intensity and $\Sigma_T I_T$ is the total transition intensity out of the level allowing for all decay paths, including internal conversion (see Section 2.5). In order

to compare experimental results with the Weisskopf estimates, an experimental reduced transition probability is evaluated, and given by [8]:

$$B_\gamma(XL) = \frac{L[(2L+1)!!]^2\hbar}{8\pi(L+1)}\left(\frac{\hbar c}{E_\gamma}\right)^{2L+1} P_\gamma(XL) \tag{1.8}$$

where $(2L+1)!! = 1 \times 3 \times 5 \times \ldots \times (2L+1)$ and E_γ is the energy of the transition given in MeV.

1.3 K-isomerism and K-forbiddenness

The nuclear states in a rotational band have lifetimes typically in the order of picoseconds [9], so a state with a half-life of more than one nanosecond is considered a long-lived state, normally referred to as an isomer. In prolate-deformed nuclei, we can see so-called K-isomers. The quantum number K, defined by $K = \Sigma_i \Omega_i$, is the sum of single-particle angular momentum projections on the symmetry axis. K is nominally conserved in nuclear transitions, but in practice, K non-conserving transitions do proceed, but are strongly retarded, and the parent states of these transitions are known as K-isomers. The decays out of K-isomers can be characterised by the degree of K-forbiddenness,

$$\nu = \Delta K - L \tag{1.9}$$

where ΔK is the change in K, and L is the multipole order of the transition. The hindrance factor, F_w of the transition is a comparison between experimental and theoretical γ-ray transitions probabilities, and is given by [7]:

$$F_w = \frac{B_w(XL)}{B_\gamma(XL)} \tag{1.10}$$

with $B_w(XL)$ and $B_\gamma(XL)$ defined in equations 1.4, 1.5 and 1.8. For transitions out of a K-isomer, one can calculate the reduced hindrance factor, f_ν by taking the ν^{th} root of F_w:

$$f_\nu = F_w^{\frac{1}{\nu}} \tag{1.11}$$

The value of f_ν was determined empirically, and found to be approximately 100 (ranging typically from 30 to 300) [11], and so each unit of ν corresponds to the transition rate being reduced by a factor of 100. Therefore, K-isomers can have unusually long lifetimes. As an example, the lowest energy state in the K=16 band of the ^{178}Hf nucleus can only decay via $\Delta K = 8$, $\Delta K = 10$, $\Delta K = 12$ and $\Delta K = 12$ transitions, which are all strongly hindered due to the large change in K leading to a state with a half-life of 31 years [12].

1.4 Decays within a Rotational Band

The M1 and E2 transition strengths between adjacent states in a rotational band may be calculated from the magnetic moment for the M1 transitions and the quadrupole moment for the E2 transitions. The rotational model [5] describes a pure E2 transition for a change in spin between initial and final states with $\Delta J = 2$, and a mixed M1/E2 transition for $\Delta J = 1$ states with the mixing ratio, δ given by these expressions:

$$\frac{\delta^2}{1+\delta^2} = \frac{2K^2(2J-1)}{(J+1)(J+K-1)(J-K-1)}\left(\frac{E_1}{E_2}\right)^2\frac{I_2}{I_1} \quad (1.12)$$

$$\frac{g_K - g_R}{Q_0} = \frac{0.933E_1}{\delta\sqrt{J^2-1}} \quad (1.13)$$

The transition energy and intensity is indicated by E and I respectively, while the subscripts 1 and 2 refer to the $\Delta J = 1, 2$ transitions respectively, between the initial and final states (see Figure 1.4).

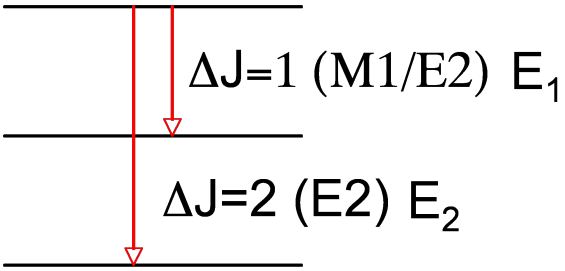

Figure 1.4: A rotational band with $\Delta J = 1$ between adjacent states. Each horizontal line represents a state in the nucleus and the decay from one state to another via γ-ray emission is indicated by arrows.

The g_K value is the *g-factor* [1] associated with the intrinsic magnetic moment, and g_R is the *g-factor* for the magnetic moment generated by the collective rotation of the nucleus. The quadrupole moment is denoted by Q_0 [14]. Since $E_1 > 0$, the sign of δ is equal to the sign of $g_K - g_R/Q_0$. The g_R value depends on the proportion of the collective angular momentum carried by the protons, and can be evaluated using the formula,

$$g_R = \frac{Z\mathcal{I}}{Z\mathcal{I}_p + N\mathcal{I}_n} \quad (1.14)$$

where Z and N are the proton and neutron number respectively, and $\mathcal{I}_{p,n}$ are the proton and neutron moments of inertia. The g_K value for a multi-quasiparticle state is related to the single-particle components by the following:

$$Kg_K = \Sigma\ \Omega g_\Omega \quad (1.15)$$

Given the value of $|g_K - g_R|/Q_0$, energies E_1, E_2 and spin J, one can calculate the branching ratio $(\frac{I_2}{I_1})$ for the $\Delta J = 1$ and $\Delta J = 2$ transitions, and mixing ratio, δ for the $\Delta J = 1$ mixed M1/E2 transitions. The reverse is also possible. With a known branching ratio, quadrupole moment and energies, the experimental value for $|g_K - g_R|$ and the M1/E2 mixing ratio (δ) can be calculated and compared with theoretical predictions to test the rotational model.

1.5 Known structure of the ^{185}Re Nucleus and Scope of the Present Work

This thesis is concerned with the structure of the nucleus ^{185}Re, which has been previously studied by Shizuma *et.al.* [15] who obtained the decay scheme shown in Figure 1.5.

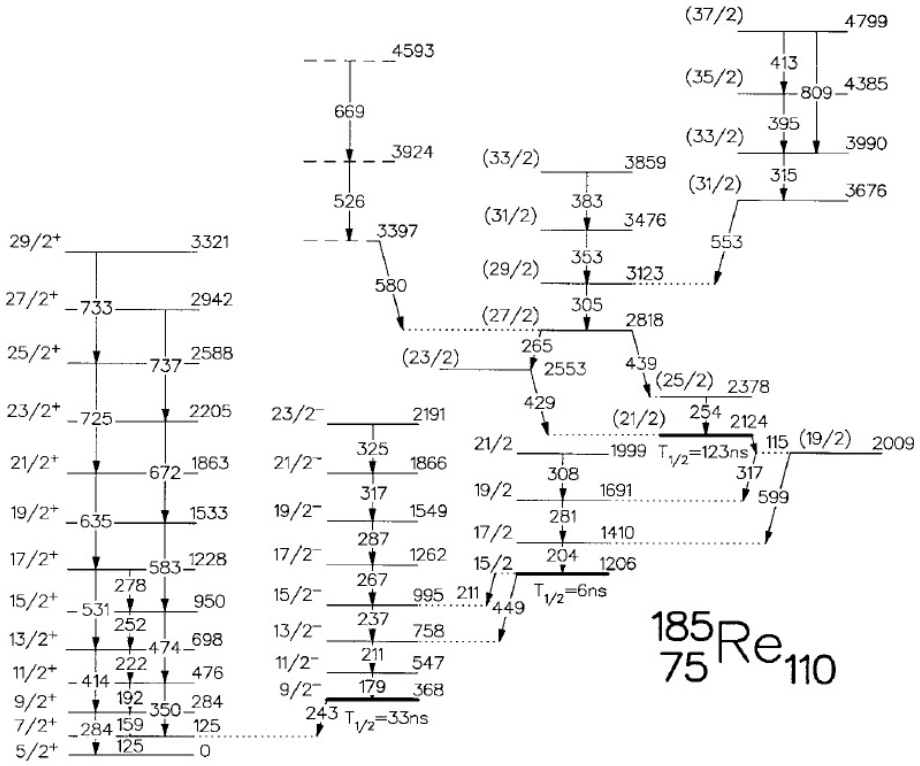

Figure 1.5: Level scheme for ^{185}Re proposed by Shizuma *et.al.* [15].

The ^{185}Re nucleus has a ground state with $K^\pi = 5/2^+$ corresponding to the single particle $5/2^+[402]$ Nilsson state from the $2d_{5/2}$ spherical parent, with a rotational band observed to spin $29/2^+$. The first single particle excited state for this nucleus is the $9/2^-[514]$ Nilsson state from the $1h_{11/2}$ spherical parent, also with a rotational band with spins observed to $23/2^-$. The E1 transition from the 33 ns isomeric state with spin $9/2^-$ to the state with spin $7/2^+$ shown in Figure 1.5 has ΔK = 2, and L = 1. The change in K is greater than the angular momentum of the decay γ-ray photon, so the transition is hindered, causing the initial state to be a K-isomer, with a half-life of 33 ns. Two further isomers have also been identified by Shizuma *et.al.* [15], with half-lives of 6 ns and 123 ns. The states immediately below the isomer at 2124 keV and every state above it do not have well defined spins and parities. Therefore, no information about the nature of these states can be obtained.

This thesis reports the extension and interpretation of the level scheme for the ^{185}Re nucleus. The ^{185}Re nucleus is stable and comprises 37.4% of natural rhenium. Excited states in ^{185}Re were populated via inelastic excitation of an enriched ^{185}Re target, and the emitted γ-rays were observed. Then, the decay scheme for ^{185}Re was deduced using

techniques of gamma-ray spectroscopy, described in the next chapter. The deduced level scheme is presented in Chapter 3, along with evidence to support the assigned configurations. Chapter 4 presents the interpretation of the new level scheme within current theoretical models of nuclear structure. Finally, Chapter 5 presents the conclusions of this work.

Chapter 2

Methods of Gamma-ray Spectroscopy

2.1 Accessing Neutron-rich Nuclei

In order to study nuclear structure, we need to make a nucleus in an excited state. This is often accomplished in heavy-ion fusion-evaporation reactions, where two light nuclei are fused to form a heavier nucleus in an excited state. Examples where such reactions were used in studying the structure of nuclei can be found in Refs. [17, 18, 19]. However, the immediate compound system is unstable, and will emit a number of nucleons. A schematic diagram for a reaction of this type is shown in Figure 2.1.

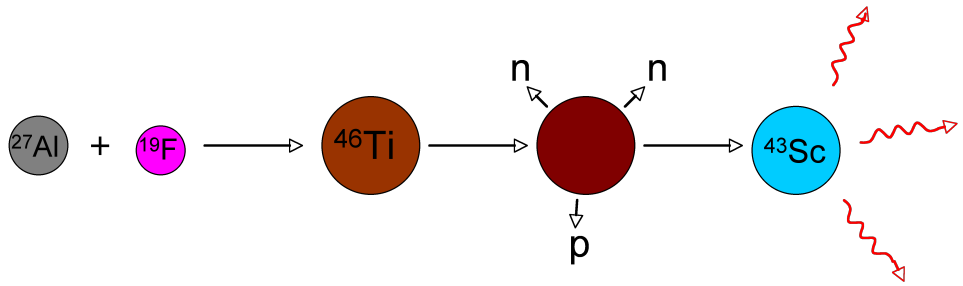

Figure 2.1: An example of a heavy-ion fusion evaporation reaction. Two nuclei, ^{27}Al and ^{19}F fuse together to form ^{46}Ti, which quickly decays to ^{43}Sc by emitting one proton and two neutrons, then further cools via emission of γ-rays.

This method is not useful in studying neutron rich nuclei since the initial compound nucleus usually emits a significant number of neutrons. Also, for stable nuclei, the neutron number N increases with the proton number Z, so fusion of two stable nuclei makes a neutron deficient nucleus. Therefore, instead of a heavy ion fusion evaporation reaction, a neutron-rich nucleus is used as a target in a deep-inelastic reaction [28, 29, 30, 31]. This type of reaction involves accelerating a beam of heavy ions to impact a stationary neutron-rich nucleus. The interaction between the beam and the target could involve multi-nucleon transfer between the two, creating new nuclei in excited states. There does not necessarily have to be nucleon exchange; as the beam can transfer some its energy to the target, effectively exciting it into a more energetic quantum state (see Figure 2.2).

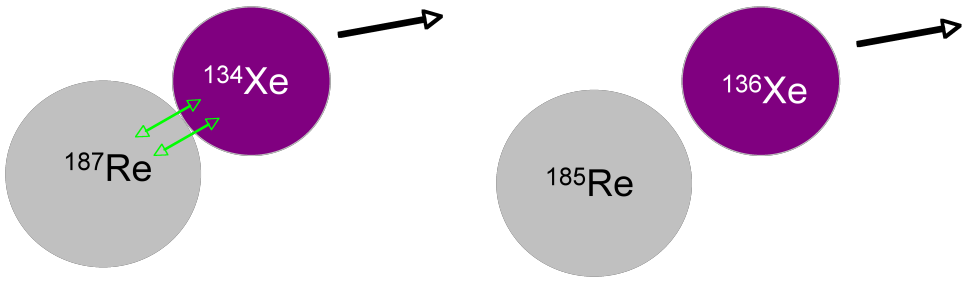

Figure 2.2: Left: A multi-nucleon transfer reaction where a ^{136}Xe beam exchanges nucleons with a stationary ^{185}Re target to form ^{134}Xe and ^{187}Re. Right: The same beam deflecting off the stationary target, leaving both ^{136}Xe and ^{185}Re in an excited state.

2.2 Gamma-ray Detection

When a nucleus is excited, it will release γ-rays to decay into a lower energy state, eventually to the ground state. These γ-rays are usually detected by large detector arrays [20, 21, 22] which consist of a large number of detectors surrounding the target nucleus. Most of the arrays around the world today utilise high-purity Germanium detectors at liquid nitrogen temperatures ($\sim$ 77 K) for γ-ray detection, connected to dedicated electronics system which provide energy and time signals for the detected γ-rays [22].

We are interested in the full energy of the γ-ray, but the γ-rays which interact with the Germanium detector do not always deposit all of their energy into the semiconductor. The most common process by which energy might be lost is Compton scattering. Therefore, the Germanium detectors are shielded by BGO scintillators (Bismuth Germanate) which supresses the Compton scattered γ-rays. So, when a γ-ray is detected by the Germanium and BGO simultaneously, it will be rejected. To avoid the γ-ray hitting the BGO scintillator directly, the BGO are shielded by Heavy Metal Collimators [22], a metal with high Tungsten composition, which is a good absorber of γ-rays. A schematic diagram of a Germanium detector shielded by BGO scintillators is shown in Figure 2.3.

2.3 Gamma-ray Spectroscopy

2.3.1 Coincidence Analysis

Nuclear decay schemes showing the transition between different states for a nucleus can be constructed by studying γ-rays emitted during its decay to the ground state. A schematic example of a decay scheme for a hypothetical nucleus is shown in Figure 2.4 with five γ-rays labelled from 1 to 5. In this imaginary nucleus, τ represents a long-lived isomeric state.

This imaginary nucleus can decay to the ground state via two possible paths. It will either decay by emitting γ_5 first, then by γ_2 and γ_1 to the ground state, or emit γ_4 and γ_3, then γ_2 and γ_1. Therefore, we can never observe γ_3 with γ_5 or γ_4 with γ_5 in an event signal. We will either observe Event 1 where γ_3 and γ_4 are emitted at the same time, then the delayed γ_1 and γ_2, or γ_5 first, then γ_1 and γ_2. From the observations of Event 1 and Event 2, we know that γ_1 is in coincidence with γ_2 and γ_3 in coincidence with γ_4, but γ_5 will never be in coincidence with γ_3 or γ_4. Thus, by knowing how the γ-rays are correlated in time, we can deduce the level structure of the nucleus, which shows the separation in energy of the quantum states and the possible γ-ray decay paths.

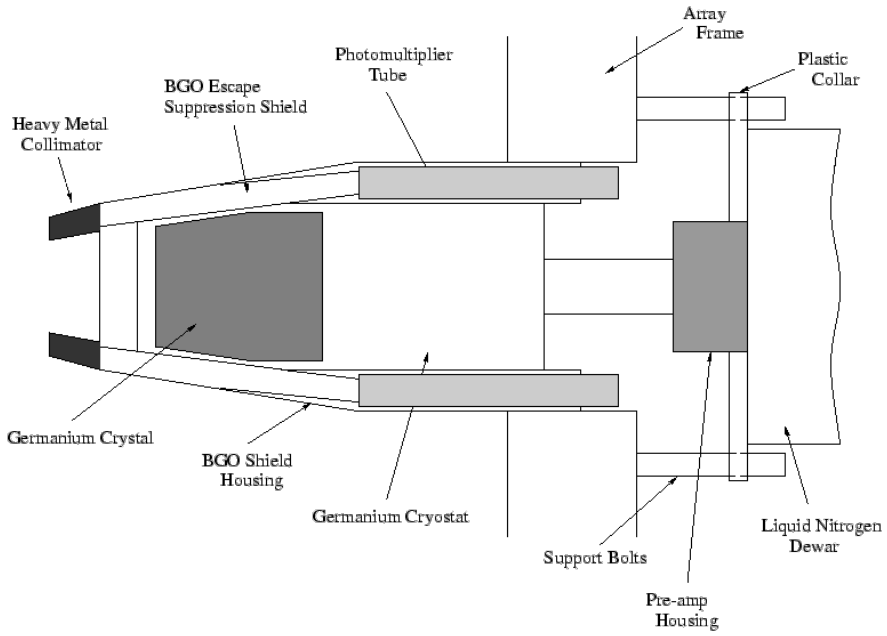

Figure 2.3: A schematic example of a γ-ray detector. The γ-rays are detected by high-purity Germanium semiconductor shielded by BGO scintillators and Heavy Metal Collimators. Diagram extracted from University of Jyväskylä Department of Physics website [23]

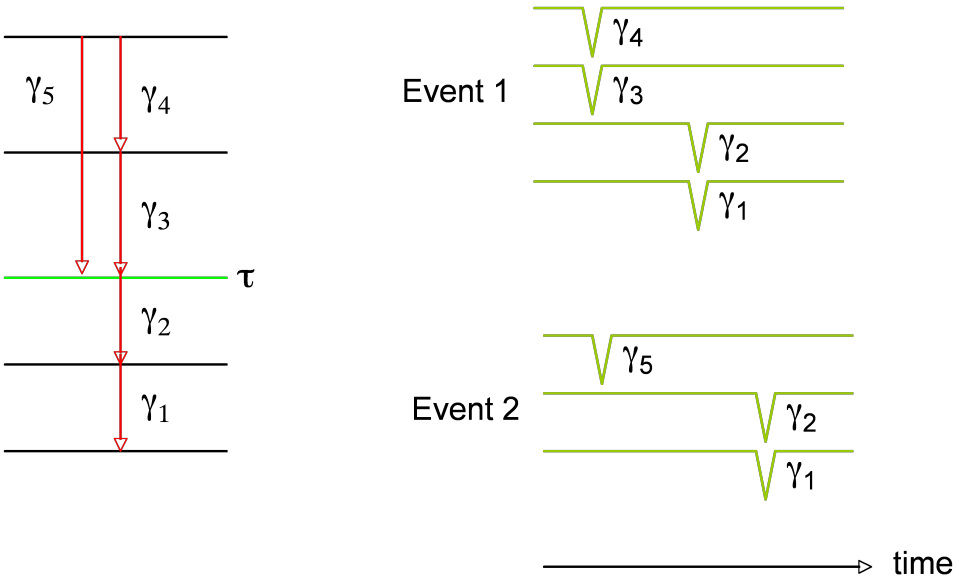

Figure 2.4: Left: A schematic example of a nuclear decay scheme including an isomer τ. Right: Example event signals for this imaginary cascade of γ-rays.

2.3.2 Prompt Coincidence

The γ-rays detected from the decay of a nucleus to its ground state can be constructed into a matrix, showing the energy and time correlations between them. An example of a γ-γ two dimensional matrix, featuring the γ-rays in Figure 2.4 is shown in Figure 2.5.

Each of the points in Figure 2.5 indicates that the γ-rays on the x and y axis were

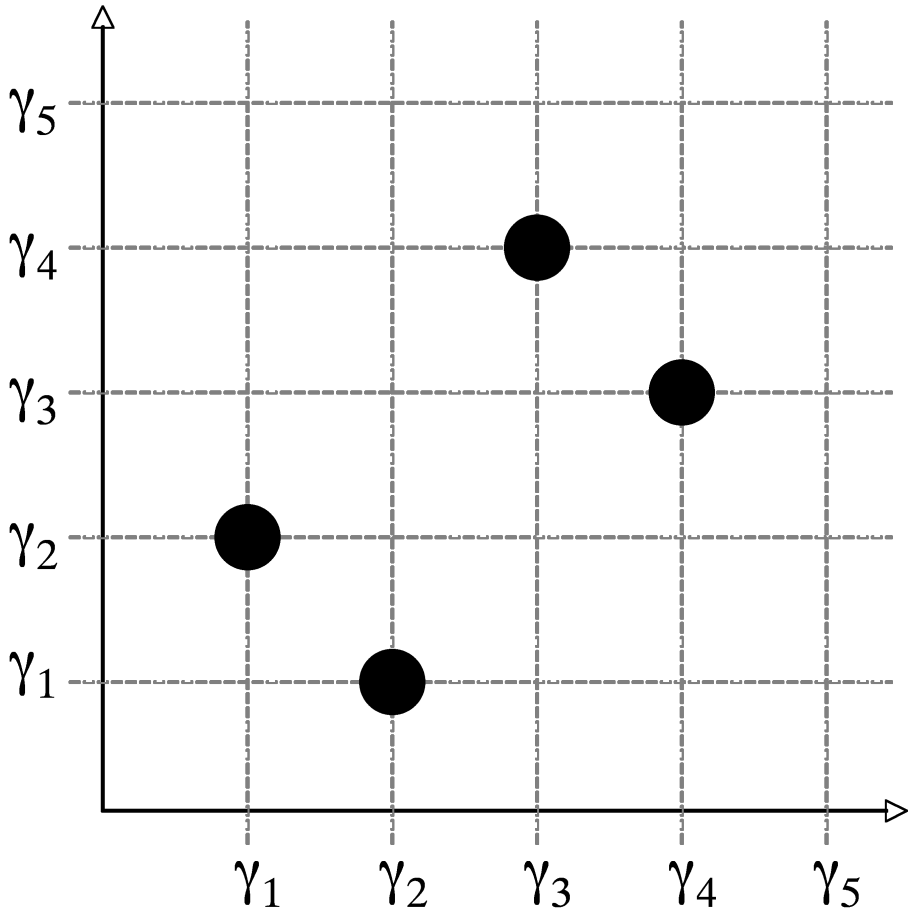

Figure 2.5: Two-dimensional γ-γ matrix illustrating prompt coincidences observed for the nuclear decay scheme shown in Figure 2.4.

detected in prompt coincidence (typically $\pm$30 ns or $\pm$140 ns). Along the diagonal, there are no points because the γ-rays in the x and y axis do not come in coincidence, unless there are two γ-rays of the same energy. This coincidence matrix will be projected onto a spectrum showing all pairs γ-rays emitted from the nucleus as shown in Figure 2.6.

Only γ-rays emitted within the coincidence overlap ($\pm$30 ns or $\pm$140 ns) are incremented, a gate on γ_5 will not see γ_3 and γ_4 since they come in parallel. Also, gates on γ_1 and γ_2 will not see γ_3, γ_4 or γ_5 if the lifetime of the isomer, τ is more than the coincidence overlap.

2.3.3 Early/Delayed Coincidence

Early coincidence analyses are performed to order γ-rays across isomeric states by constructing an early-delayed matrix with the increment of γ-rays depending on their relative time of detection. The matrix is not symmetric in this case, and is illustrated in Figure 2.7 and Figure 2.8 where the points indicate the existence of early-delayed relationships between the γ-rays in the x and y axes. In the early-delayed matrix, the y-axis is early, and the x-axis is delayed (see Figure 2.7). If we gate on the γ-rays in the delayed axis, we will only see the early γ-rays (above the isomer) . We would expect the opposite in the delayed-early matrix. If we gate on the γ-rays in the early axis, we will only see the delayed γ-rays (below the isomer).

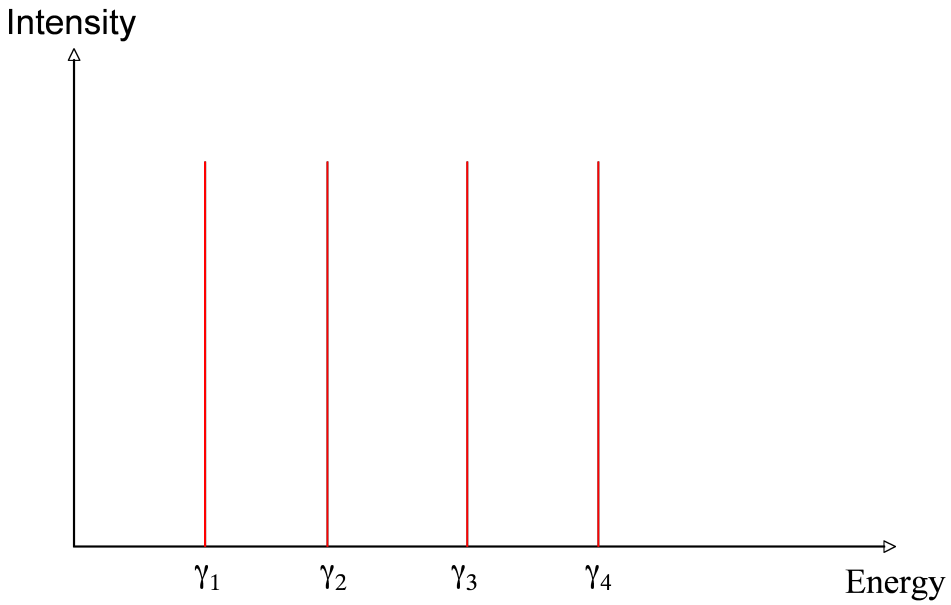

Figure 2.6: Full projection of prompt γ-γ coincidence matrix

If there are no isomers in the cascade, the order of the transitions may be determined by considering that there could be more than one γ-ray which depopulate an excited state. For example, assume that the isomer did not exist in Figure 2.4 and the order of $\gamma_1, \gamma_2, \gamma_3$ and γ_4 is known. Then, the position of γ_5 is assigned based on the information that $\gamma_3 + \gamma_4 = \gamma_5$.

2.4 Lifetime Analysis

2.4.1 Pulsed Beam

If the beam is pulsed, long-lived states will decay in the time between beam pulses. If the time period between the pulses is longer than the lifetime of an isomeric state in the nucleus, the half-life of that isomer can be determined by measuring the drop in intensity between beam pulses. In the context of Figure 2.4, the aforementioned γ-rays will be γ_1 and γ_2, for a measurement of the half-life of the isomer τ. The intensity, I of these γ-rays decrease with time, t according to the radioactive decay law [1]:

$$I = I_0 e^{-\frac{t}{\tau}} \tag{2.1}$$

where I_0 is the initial intensity and τ is the meanlife of the decay. The half-life, $T_{1/2}$ and meanlife, τ are related by the following equation:

$$T_{1/2} = \tau ln2 \tag{2.2}$$

2.4.2 Relative Time

An alternative method for measuring the lifetime of isomers is by determining the time difference between detection of two γ-rays which decay with an isomer in between. This time difference may be obtained by sorting the coincidence data into a three-dimensional γ-γ-*time* matrix, with the two γ-ray energies on the y and z axes, and the time difference

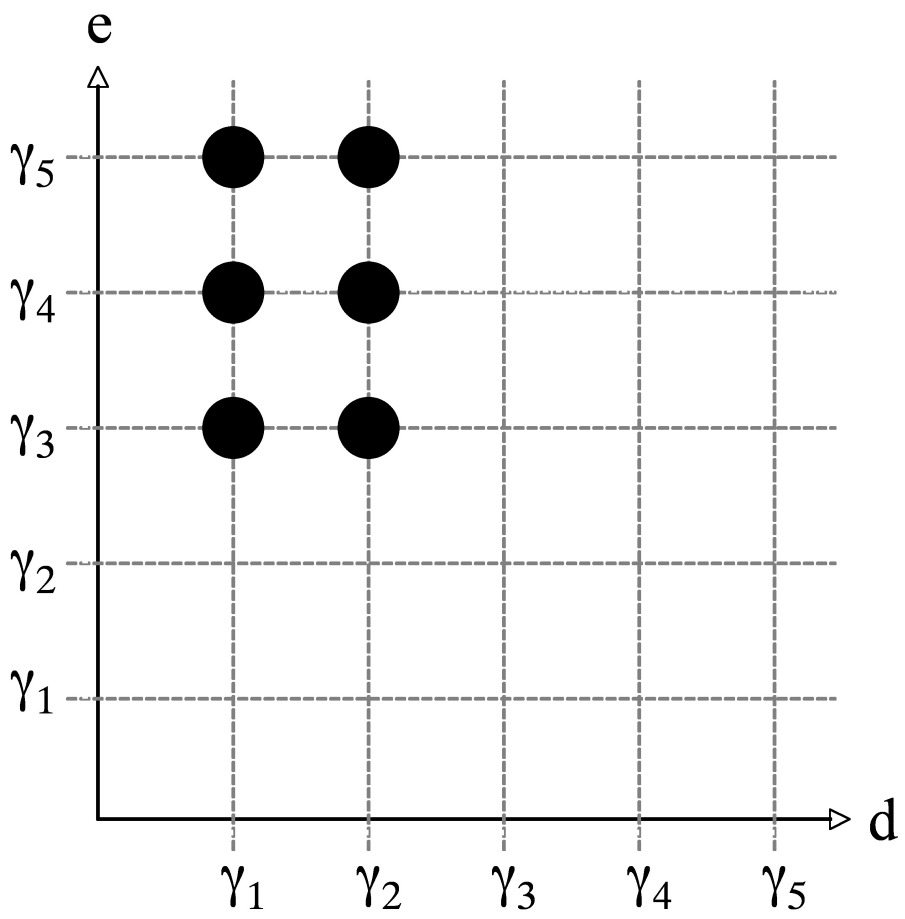

Figure 2.7: An early-delayed matrix. The y-axis is early (γ-rays above the isomer), and the x-axis is delayed (γ-rays below the isomer).

between them on the x-axis. From the example in Figure 2.4, the lifetime of the isomer τ can be determined by gating on γ_5 and γ_2 on the y and z axes and projecting them into the x-axis. We will refer to this as the (γ_5,γ_2) slice. It will show a positive time difference because γ_5 is above the isomer and γ_2 is below it. The opposite slice, (γ_2,γ_5), will show a negative time difference. A schematic example showing a positive and negative time difference is shown in Figure 2.9.

2.5 Internal Conversion

Another transition process which can occur is internal conversion, where the transition energy is absorbed by an atomic electron, which is then expelled from the atom with an energy equal to the transition energy minus the electron binding energy. The intensity ratio between the emission of a conversion electron and a γ-ray is known as the conversion coefficient, α_T, given by

$$\alpha_T = \frac{I_e}{I_\gamma} \tag{2.3}$$

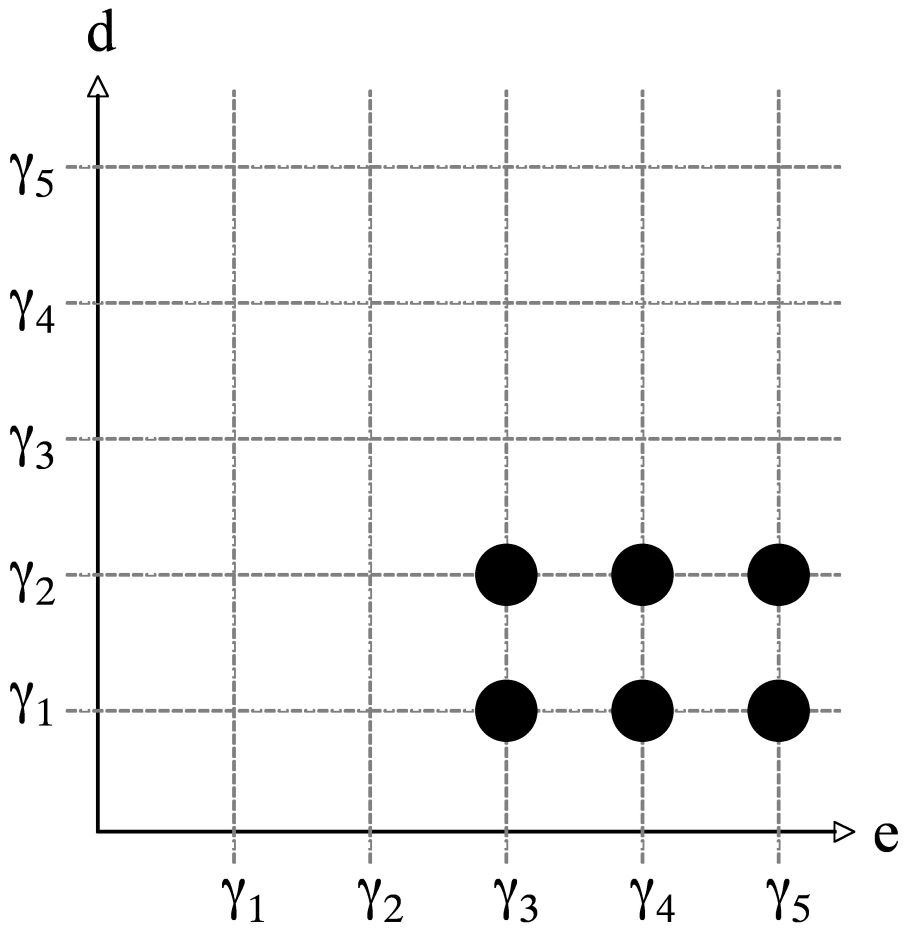

Figure 2.8: A delayed-early matrix. The y-axis is delayed (γ-rays below the isomer), and the x-axis is early (γ-rays above the isomer).

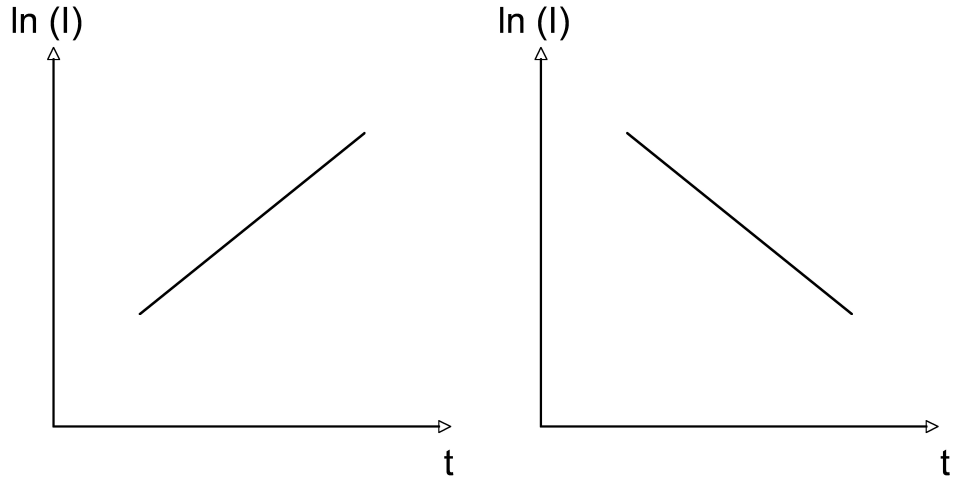

Figure 2.9: Left: A positive time difference spectrum. Right: A negative time difference spectrum

where I_e and I_γ are the intensities of the conversion electron and the γ-ray respectively. The conversion coefficient is a function of both the transition energy and the multipolarity [24, 32], hence a measurement of the conversion coefficient can be used to determine

the multipolarity of the transition.

2.6 Real Life Analysis

2.6.1 Energy spectra

The methods of coincidence analyses described so far have been stylised for simplicity. In reality, the intensities observed in a γ-ray spectrum do not reflect the true intensity of the transition. An excited nucleus can release its energy via internal conversion (described in the Section 2.5), therefore the γ-ray intensity observed is not the true transition intensity. Furthermore, the detectors are not 100% efficient, and their efficiencies are γ-ray energy dependent. Also, the resolution of the detectors are not perfect, so the peaks observed in a γ-ray spectrum are broadened with a Gaussian profile.

However, the transition intensity can still be determined by taking into account the detector efficiencies and internal conversion. First, the area of the γ-ray peak is measured. Then, it is divided by the efficiency of the detectors for that particular γ-ray energy to obtain the intensity of the γ-ray. Finally, a factor of one plus the internal conversion is added. This is illustrated in the following equations:

$$I_\gamma = \frac{peak\ area}{efficiency} \tag{2.4}$$

$$I_T = I_\gamma(1 + \alpha_T) \tag{2.5}$$

where I_γ and I_T are the γ-ray and transition intensities, and α_T is the internal conversion coefficient, determined by the transition energy and the atomic number of the nucleus [32]. This technique to measure the total transition intensity could be used to determine the conversion coefficient, and hence the multipolarity of a particular transition. The intensity of transitions which enter a state must be the same as the intensity of the exiting transitions, by conservation of energy. Then, a balance on the intensities of the entering and exiting transitions can enable us to deduce the conversion coefficient of a transition with an unknown multipolarity.

Moreover, there are often contaminants from other sources, and therefore the actual background is not always as clean as shown in the schematic γ-ray spectra. The effective background can be reduced by extending the coincidence analysis to three [33], four and higher dimensions, which includes the construction of γ-γ-γ, γ-γ-γ-γ, and higher dimensional coincidence cubes [34]. This enables more than one gate to be set on the γ-ray spectra. Some of the contaminants which come in coincidence with one of the γ-rays in the nucleus might not come in coincidence with two or three γ-rays in the nucleus. Therefore, higher dimensional gates will isolate γ-rays in the nucleus much more effectively, hence making it easier to deduce the level structure.

2.6.2 Time Spectra

The relative time difference spectra shown in Figure 2.9 are idealised, showing only lines with noticable slopes. In practice, noise from contaminants will be present in the background. Furthermore, we will see the time response of the detector in a relative time spectrum instead of a straight line. An example of what a positive relative time spectrum might look like is shown in Figure 2.10.

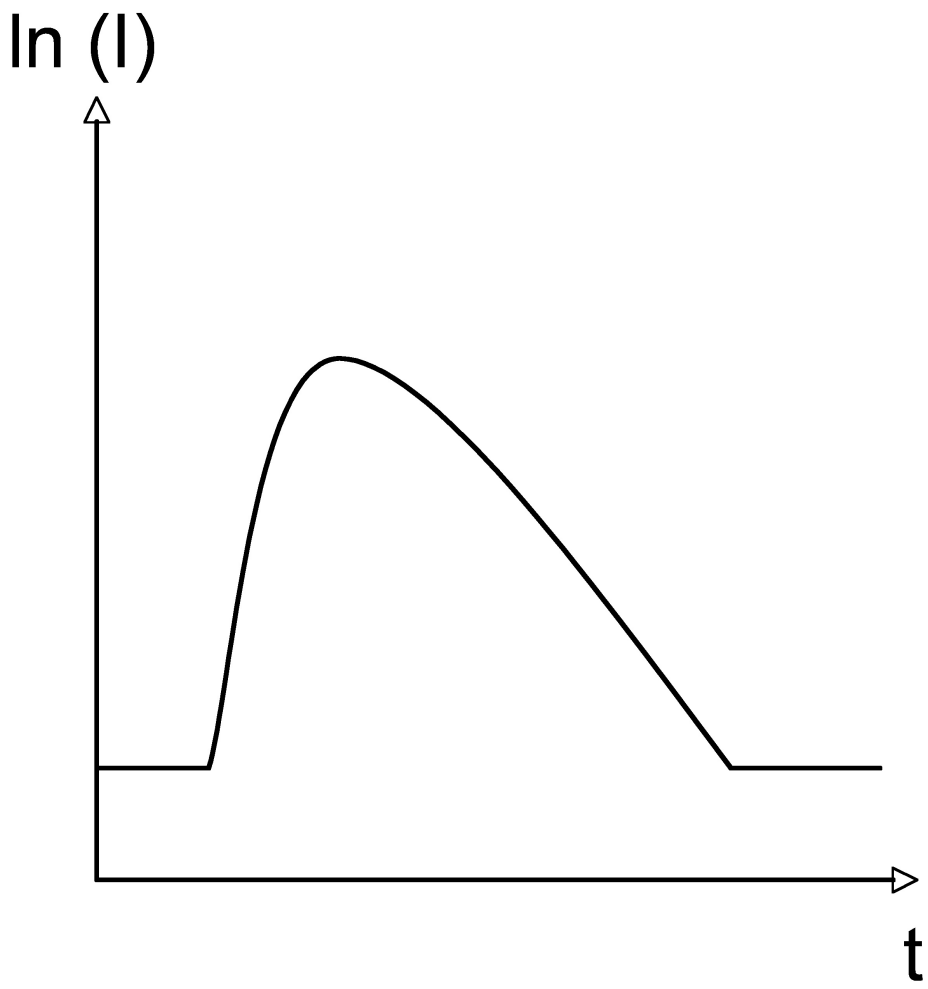

Figure 2.10: An example of an actual positive relative time spectrum

The meanlife is determined by fitting a theoretical decay curve, $F(x,\tau)$ [16] to the experimental curve. The analytical expression for the decay curve is shown in equation 2.6:

$$F(x,\tau) = [(2\pi)^{1/2}\sigma]^{-1} \int_{\infty}^{x} \frac{1}{\tau} e^{[\frac{1}{\tau}(y-x)-\frac{(y/\sigma)^2}{2}]}\, dy \tag{2.6}$$

where x and y symbolises the axes of the spectrum and σ is the full width at half maximum (FWHM) of the time response.

In the case where the meanlife is much less than the full width at half maximum (FWHM) of the time response curve, the meanlife can be obtained from the shift in the centroid. This shift is determined by overlaying the positive and negative time difference spectra and measuring the difference between the two peaks, as illustrated in Figure 2.11. The difference is twice the meanlife.

The shape of the time response curve is also energy dependent, since γ-rays with low energies cannot penetrate deep enough into the central detection structure of the Germanium detector. Therefore, γ-rays with low energies are intrinsically delayed due to slower charge collection times, showing a detectable "walk" in the time response curve. An example of this can be seen in Figure 3.18 in Chapter 3.

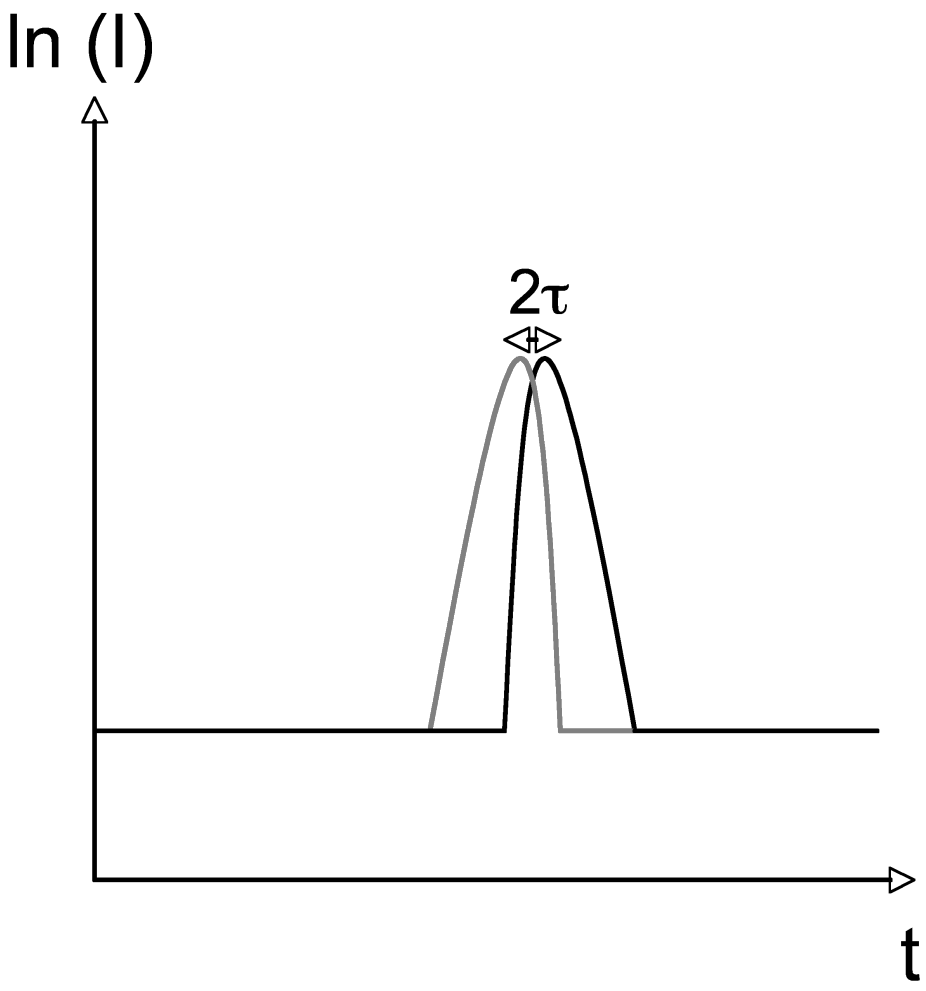

Figure 2.11: Measurement of a short meanlife using a centroid analysis. The difference between the peaks is twice the meanlife.

2.7 Angular Correlations

The intensity of a γ-ray transition has an angular dependence on the transition multipolarity and direction of the nuclear spin. In a conventional heavy-ion fusion evaporation reaction where the projectile nucleus fuses with the target nucleus, the spin of the final product is aligned in a plane perpendicular to the beam direction [25]. Therefore, the angular intensity depends on the angle of emission with respect to the beam axis.

There is less spin alignment in deep-inelastic reactions, where the beam-like fragments can scatter in many directions. Furthermore, hyperfine interactions between the nucleus and its environment can dealign the spin, and less angular momentum alignment remains overtime. As a result, γ-rays emitted after the decay of a long-lived isomer can be generally assumed to have no spin alignment, in deep-inelastic reactions.

However, observing a γ-ray at a particular angle implies that the nucleus is more likely to have the spin pointing in some particular direction, effectively "aligning" the nuclear spin. Thus, observing a second γ-ray at some angle $\Delta\theta$ to the first, will have different probabilities W [26, 27], which depend on $\Delta\theta$.

If the detectors are grouped according to the angular difference between them, the

probabilities W($\Delta\theta$) can be measured from coincidence intensities between γ-rays. Then, the results are compared with theoretical predictions for the angular behaviour dependent on the transition multipolarities and nuclear spins [1, 25]. These probability curves are known as angular correlations and theoretical predictions [27] are shown in the figures below. The spins used are arbitary, as only the difference in spin between the initial and final states matter. The expected angular correlation between a stretched E1 or E2 transitions [25] and transitions of various multipolarities are shown in Figure 2.12. Figure 2.13 and Figure 2.14 shows the calculated angular correlation curves between a mixed M1/E2 transition and stretched ($L = \Delta J$) or unstretched ($L > \Delta J$) E2 transition. The curves shown in Figure 2.15 are the correlations between mixed M1/E2 transitions with various mixing ratios. The curves were produced by Dr. Greg Lane, using the DCOPLOT program developed by Dr. Andrew Stuchbery from the Department of Nuclear Physics.

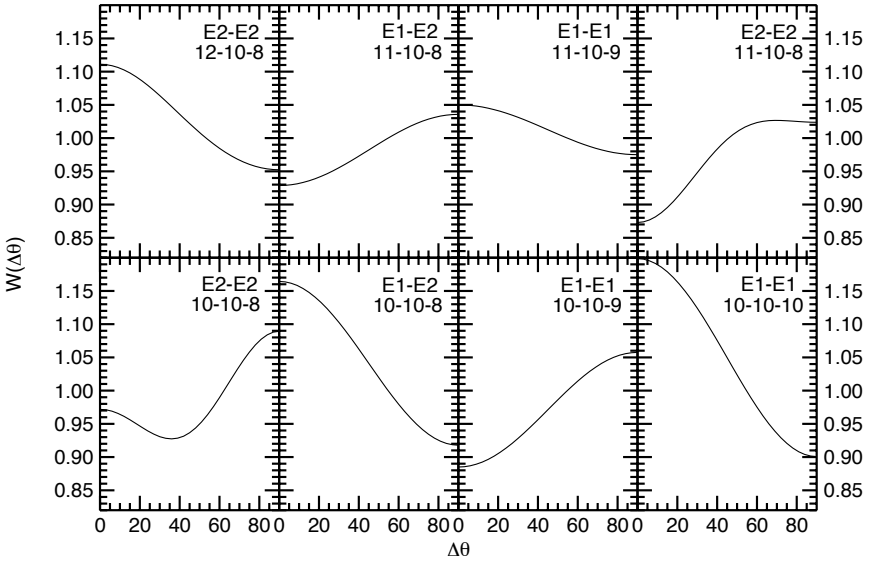

Figure 2.12: Angular correlation curves between various combinations of stretcthed ($L = \Delta J$) and unstretched E1 or E2 transitions and various multipolarities calculated for the different marked spin sequences.

The angular correlation curves which include unstretched E1 and stretched E2 transitions show negative slopes overall, while the curves which include stretcthed E1 and stretched E2 transitions have overall positive slopes. The curves for unstretched E2 transitions have completely different shapes, with mixture of negative and positive slopes.

The curves for the angular correlation between mixed M1/E2 transitions with negative mixing ratio and pure E2 transitions have positive slopes overall, with the anisotropy decreasing as the magnitude of the mixing ratios decrease.

The curves for the angular correlation between mixed M1/E2 transitions with negative mixing ratio and pure E2 transitions have negative slopes overall, with the exception of the curve where the mixing ratio is +0.1, which is quite flat. Nevertheless, there is a

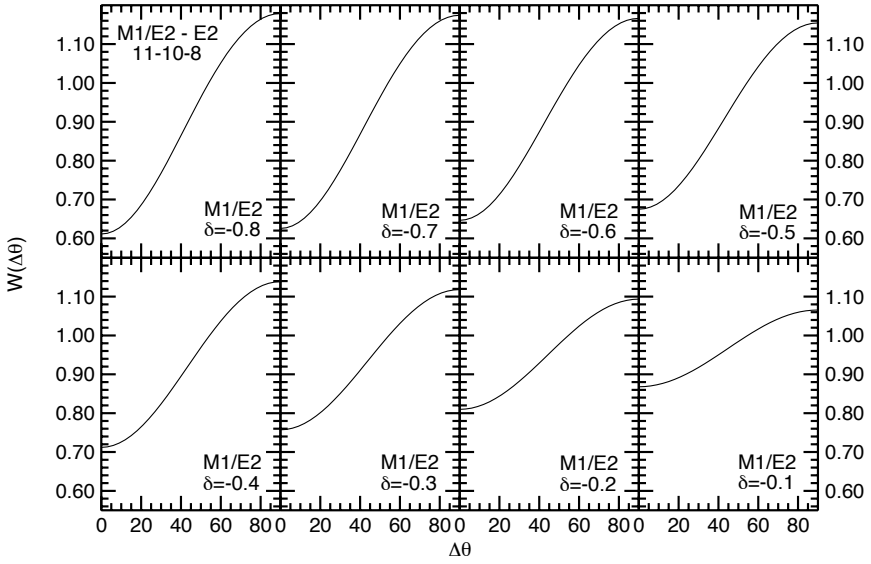

Figure 2.13: Angular correlation curves between an E2 transition and M1/E2 transition with various negative mixing ratios calculated for the spin sequence of $11 \longrightarrow 10 \longrightarrow 8$.

general trend where the anisotropy inceases with increasing magnitude of mixing ratios.

The curves for the angular correlation between mixed M1/E2 transitions where both the mixing ratios are positive (Figure 2.15) have negative slopes overall, with the anisotropy increasing for larger mixing ratios. However, the curve which include a mixing ratio of zero (indicating a pure transition) for one of the transitions show positive slopes overall. There is still a similar trend where the anisotropy increases as the the mixing ratios get larger.

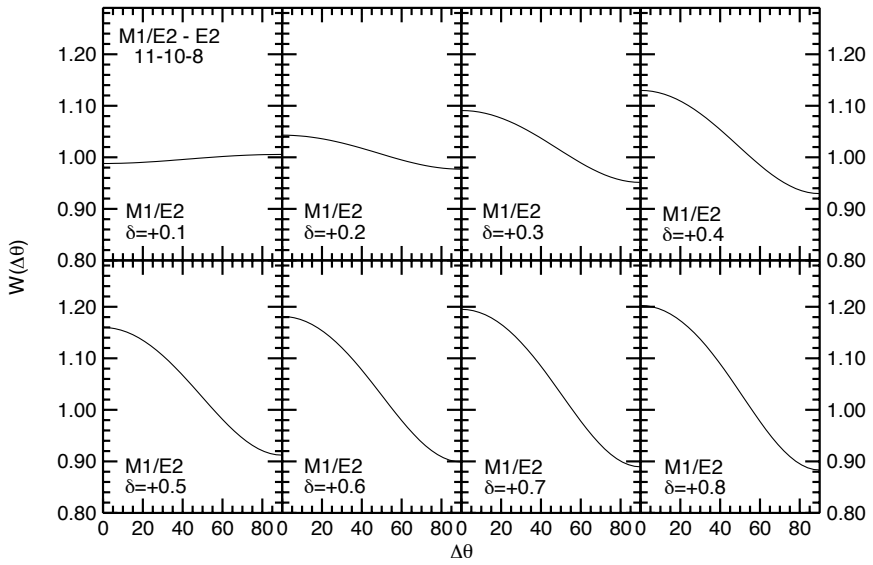

Figure 2.14: Angular correlation curves between an E2 transition and M1/E2 transition with various positive mixing ratios calculated for the spin sequence of $11 \longrightarrow 10 \longrightarrow 8$.

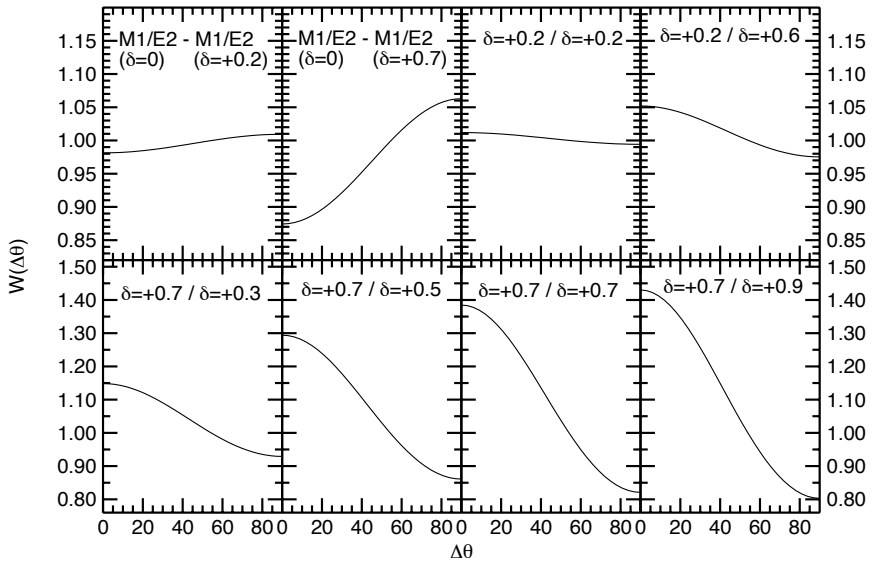

Figure 2.15: Angular correlation curves between mixed M1/E2 transitions with various mixing ratios.

Chapter 3

Results

This chapter describes the experimental results for the investigation of the structure for ^{185}Re using the techniques of γ-ray spectroscopy described in the previous chapter.

3.1 Data Acquisition

An extensive data set containing information on ^{185}Re already existed as a part of a program of experiments performed at Argonne National Laboratory (ANL) by a collaboration which included The Australian National University (ANU), ANL, and University of Massachusetts Lowell (UML), and led by Dr. Filip Kondev (ANL), Prof. George Dracoulis (ANU), and Dr. Greg Lane (ANU). These experiments were performed mainly to study the structure of neutron-rich nuclei [28, 29, 30, 31]. The experiment which allows the structure of the ^{185}Re nucleus to be probed was performed in November 2004 and used nanosecond pulsed 820MeV ^{136}Xe beams separated by 825 ns, provided by the ATLAS accelerator facility [35], incident on a gold-backed 97% enriched ^{185}Re target. Excited states in ^{185}Re were populated via inelastic excitation and the γ-rays emitted by excited ^{185}Re nuclei were detected by the Gammasphere array [22] (see Figure 3.1), which consists of up to 110 Compton-uppressed Germanium detectors which covers 4π solid angle with 48% Germanium coverage. For this experiment, 98 detectors were operational.

A total of 1.8×10^9 events with at least 3 suppressed γ-rays were collected on EXABYTE data tapes. Some pre-existing analysis had already been performed by Dr. Greg Lane from the Department of Nuclear Physics, including gain and time-matching of the individual detectors, and subsequent sorting into a database [34]. The data were sorted into various matrices and cubes, of which the following conditions were used for the starting analysis:

1. out-of-beam(>100 ns after the beam pulse) γ-γ-γ cube with prompt relative time condition of $\pm$140 ns
2. in-beam (within 100 ns of beam pulse) prompt γ-γ-γ cube.
3. early-delayed matrices with 30-50 and 150-800 ns time ranges
4. $\gamma - \gamma - time$ cube for the out-of-beam region (> 100 ns after the beam pulse)

3.2 New States Below the 2124 keV Level

The out-of-beam cube with a prompt relative time condition of $\pm$140 ns has been analysed. A total of nine new γ-rays, two new states and one new isomer were found, and placed

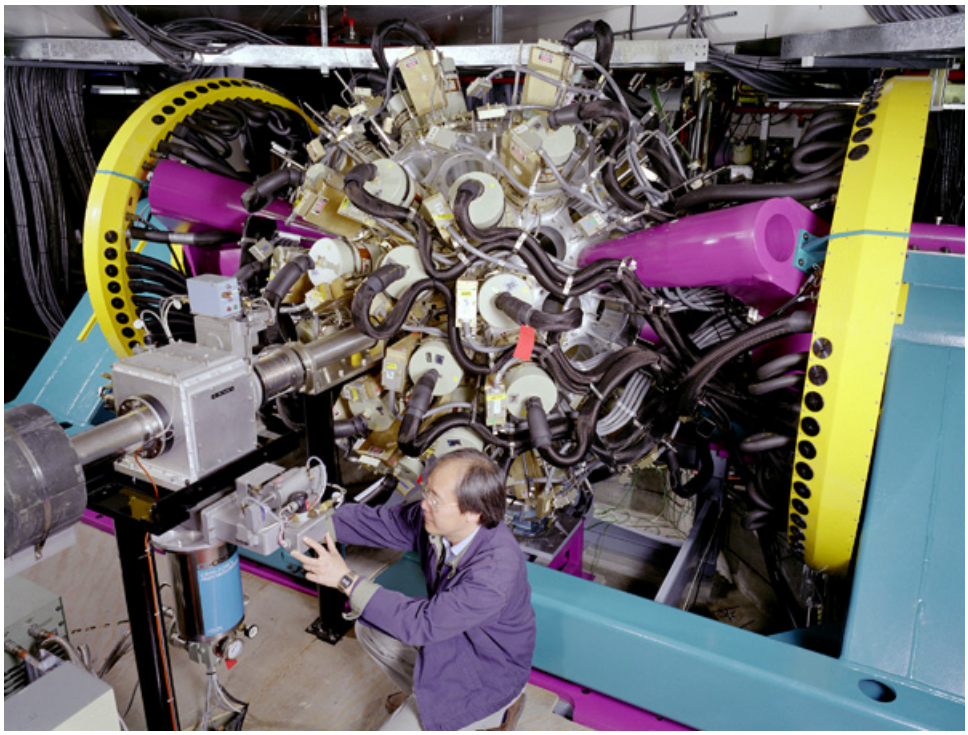

Figure 3.1: Gammasphere consisting of up to 110 Compton-suppressed Germanium detectors

below the 2124 keV state. Figure 3.2 shows the new level scheme, where the width of the arrows are proportional to the intensities of the transitions. Table 3.1 lists the energies (E_γ) and intensities (I_γ) for all transitions fed by the 2124 keV state. The uncertainty in the last digits for each measured value are shown in brackets.

Coincidence spectra from the double gate on the 243 and 125 keV γ-rays shows γ-rays not observed by Shizuma *et. al.* [15]; with energies 98, 174, 390, 561, 589, 659, and 741 keV. The 561, 659, and 741 keV γ-rays were found to be parallel to the 449 keV γ-ray from their absence in the spectrum when double gating on the 243 and 449 keV γ-rays, and the disappearance of the known 179 and 211 keV γ-rays from the 243/741 spectrum pinpoints their position in the level scheme.

The existence of the 390 keV transition was established by its disappearance in the 179/243 and 211/243 keV double gates, and the absence of the 179 and 211 keV γ-rays in the 390/243 keV double gate confirms its position (see Figure 3.4). There is another 448 keV transition in the rotational band from the $9/2^-[514]$ Nilsson single particle state. It was deduced from a significant 448 keV peak in the 267/287 double gate from the in-beam $\gamma-\gamma-\gamma$ cube (see Figure 3.5). The 589 keV transiton was added to the scheme from the disapearance of the 281 and 308 keV γ-rays in the 589/243 double gate. This is confirmed by the absence of the 589 keV γ-ray in the 281/243 and 308/243 coincidence spectra (see Figure 3.6). The position of the 98 keV transition was deduced to be parallel to all of the 211, 448 and 659 keV transitions from the disappearances of the 211, 448 and 659 keV γ-rays in the 98/243 double gate. This is supported by the 448/243 and the 659/243 double gates, as the 98 keV γ-ray was not observed in either spectrum (see Figure 3.8).

The 173keV transition was found to be parallel to the 204keV transition from the 173/243 and 204/243 coicidence spectra (see Figure 3.7) and the existence of the 31keV transition was inferred, but cannot be observed because the 31 keV transition is low

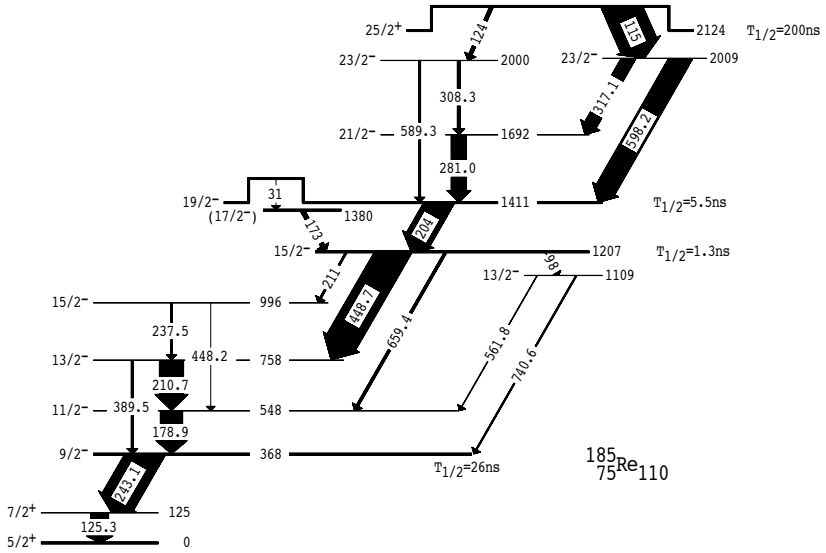

Figure 3.2: New level scheme for states fed by the 2124 keV state.

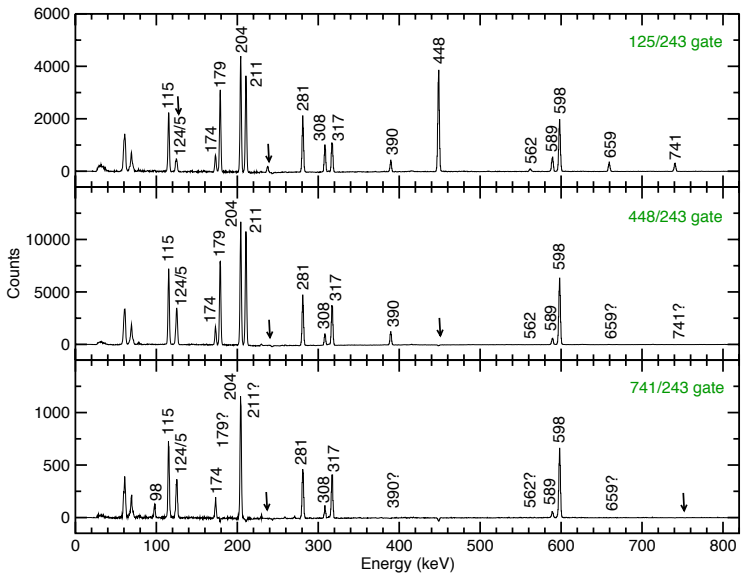

Figure 3.3: Prompt coincidence spectra double gated on the 125/243, 448/243 and 741/243 keV γ-ray pairs from the out-of-beam cube. The arrows show which γ-rays are gated.

in energy, therefore most of the energy of this transition was released through internal conversion to an atomic electron.

The existence of these γ-rays is supported by spectra which shows γ-rays delayed with respect to the 254 keV transition which feeds the isomer at 2124 keV (see Figure 3.9).

E_γ (keV)	I_γ	$J_i^\pi \longrightarrow J_f^\pi$
97.8 (2)	7 (1)	$15/2^- \longrightarrow 13/2^-$
115.2 (2)	1000 (150)	$25/2^+ \longrightarrow 23/2^-$
123.8 (2)	131 (13)	$25/2^+ \longrightarrow 23/2^-$
125.3 (8)	425 (37)	$7/2^+ \longrightarrow 5/2^+$
173.1 (2)	119 (6)	$17/2^- \longrightarrow 15/2^-$
178.9 (2)	580 (29)	$11/2^- \longrightarrow 9/2^-$
204.2 (2)	704 (35)	$19/2^- \longrightarrow 15/2^-$
210.7 (2)	625 (110)	$13/2^- \longrightarrow 11/2^-$
211.2 (5)	52 (5)	$15/2^- \longrightarrow 15/2^-$
237.5 (5)	50 (3)	$15/2^- \longrightarrow 13/2^-$
243.1 (2)	921 (46)	$9/2^- \longrightarrow 7/2^+$
281.0 (2)	401 (20)	$21/2^- \longrightarrow 19/2^-$
308.3 (2)	88 (4)	$23/2^- \longrightarrow 21/2^-$
317.1 (2)	345 (17)	$23/2^- \longrightarrow 21/2^-$
389.6 (2)	66 (3)	$13/2^- \longrightarrow 9/2^-$
448.2 (5)	5 (1)	$15/2^- \longrightarrow 11/2^-$
448.7 (2)	848 (127)	$15/2^- \longrightarrow 13/2^-$
561.8 (2)	19 (3)	$13/2^- \longrightarrow 11/2^-$
589.3 (2)	51 (8)	$23/2^- \longrightarrow 17/2^-$
598.2 (2)	548 (82)	$23/2^- \longrightarrow 17/2^-$
659.4 (2)	74 (11)	$15/2^- \longrightarrow 11/2^-$
740.6 (2)	52 (8)	$13/2^- \longrightarrow 9/2^-$

Table 3.1: Energies and intensities of γ-rays below the 2124 keV level. J_i^π and J_f^π are the initial and final spins and parities respectively. The intensities are calculated relative to the strongest transition of 115 keV fixed at 1000.

3.3 New States Above the 2124 keV Level

All pairs of clean double gates in the out-of-beam region were organised into a group of gates. Pairs of γ-rays which precede both the γ-rays from any pair of γ-rays in the group by 30-800 ns were incremented if they were in prompt coincidence within $\pm$140 ns. The projection of this is shown in Figure 3.10. The γ-ray decay scheme proposed by Shizuma *et. al.* [15] (see Figure 1.5) for the structure above the isomer at 2124 keV has been modified from the coincidence analyses performed on this projection. The new scheme is shown in Figure 3.11. The width of the arrows are not proportional to the transition intensities as in the case of Figure 3.2 since they have not been measured due to time constraints.

T. Shizuma *et. al.* [15] observed a transition from the 4799 keV level to the 3990 keV level at 809 keV (see Figure 1.5). However, this γ-ray was not observed in the present work. Also, the 383 keV transition observed by T. Shizuma *et. al.* [15] from the 3859 keV level to the 3476 keV level could not be confirmed as a transition in ^{185}Re because the data was contaminated with a transition in ^{136}Xe (the heavy ion beam used in the experiment described in Section 3.1) which has an energy of 381 keV [36]. The 381 keV γ-ray is often strong and always present in the current (prompt) data. For instance, it has a strong intensity in the 267/287 double gate shown in Figure 3.5 from the in-beam cube.

T. Shizuma *et. al.* [15] observed a transition from the 3397 keV level to the 2818 keV level at 580 keV, in parallel with the 305 keV transition from the 3123 keV level to the

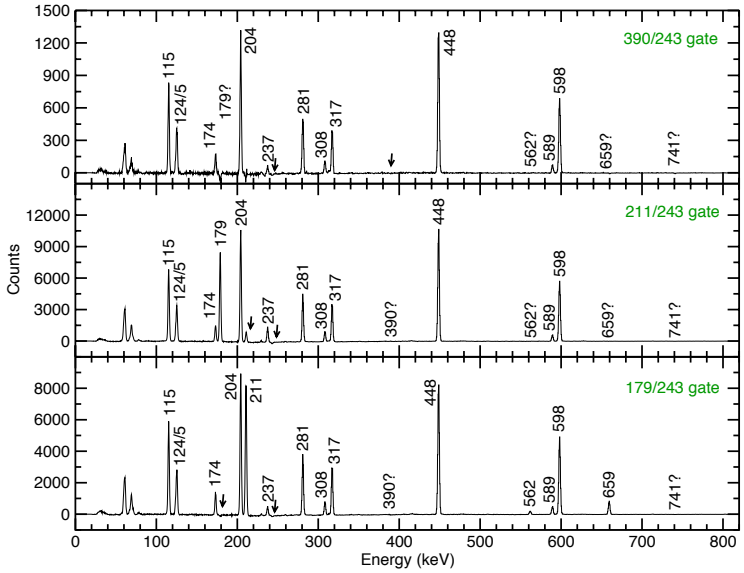

Figure 3.4: Prompt coincidence spectra double gated on the 390/243, 211/243 and 179/243 keV γ-ray pairs from the out-of-beam cube.

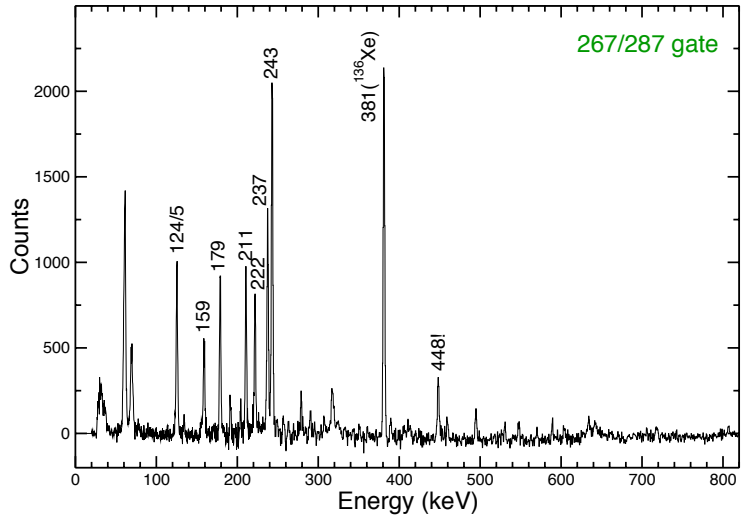

Figure 3.5: Prompt coincidence spectrum double gated on the 267 and 287 keV γ-rays from the in-beam cube.

2818 keV level. However, the 580 keV γ-ray cannot be parallel to the 305 keV transition because it is observed in the 305 keV gate, and vice versa (see Figure 3.12). Therefore, the order of the 526 keV transition, previously observed by T. Shizuma *et. al.* [15] from the 3924 keV level to the 3397 keV level and the 580 keV transition observed by T. Shizuma *et. al.* [15] from the 3397 keV level to the 2818 keV level were swapped (see Figure 3.11.

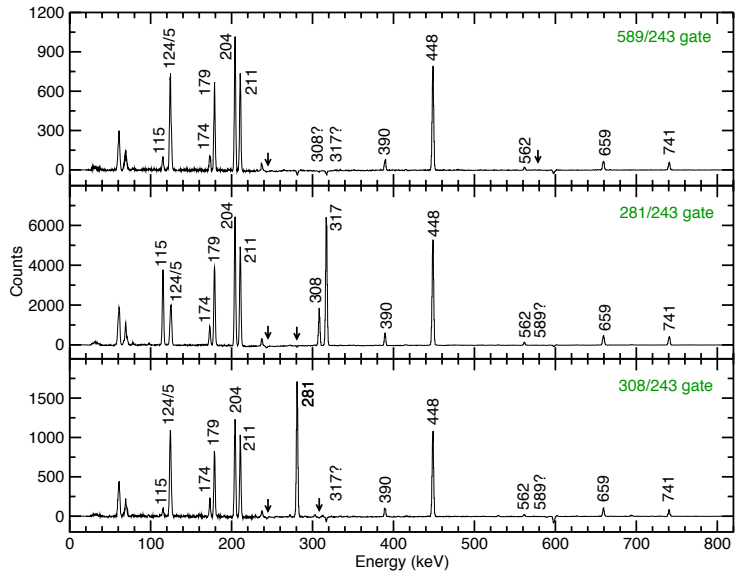

Figure 3.6: Prompt coincidence spectra double gated on the 589/243, 281/243 and 308/243 keV γ-ray pairs from the out-of-beam cube.

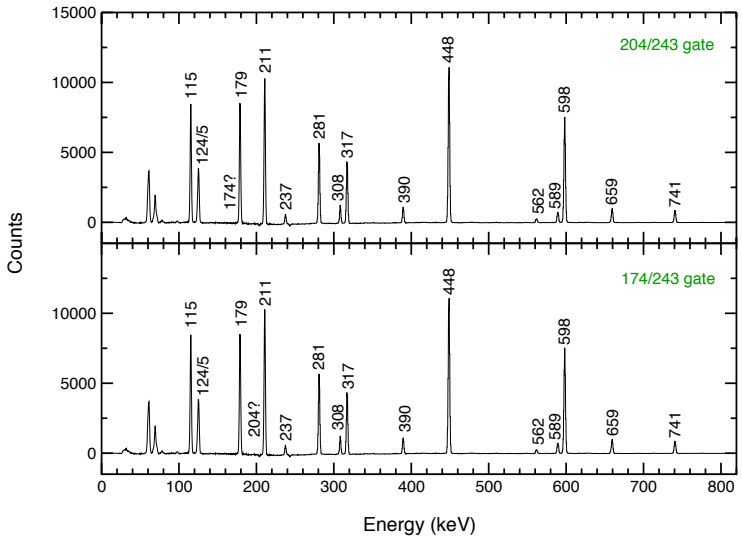

Figure 3.7: Prompt coincidence spectra double gated on the 204/243 and 174/243 keV γ-ray pairs from the out-of-beam cube.

The gate on the 580 keV γ-ray shows discrepancies between the experimental data and the existing level scheme by T. Shizuma *et. al.* [15]. The 315 keV γ-ray is observed with a significant intensity even though there is no path which connects the 580 keV transition with the 315 keV transition.This leads to the hypothesis of another 580 keV transition, parallel to the first 580 keV transition because the 580 keV gate does not show a 580 keV

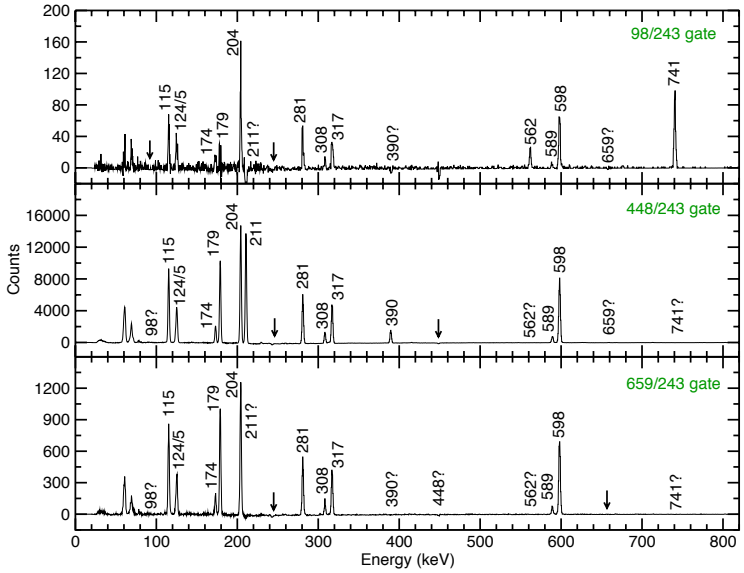

Figure 3.8: Prompt coincidence spectra double gated on the 659/243, 448/243 and 98/243 keV γ-ray pairs from the out-of-beam cube.

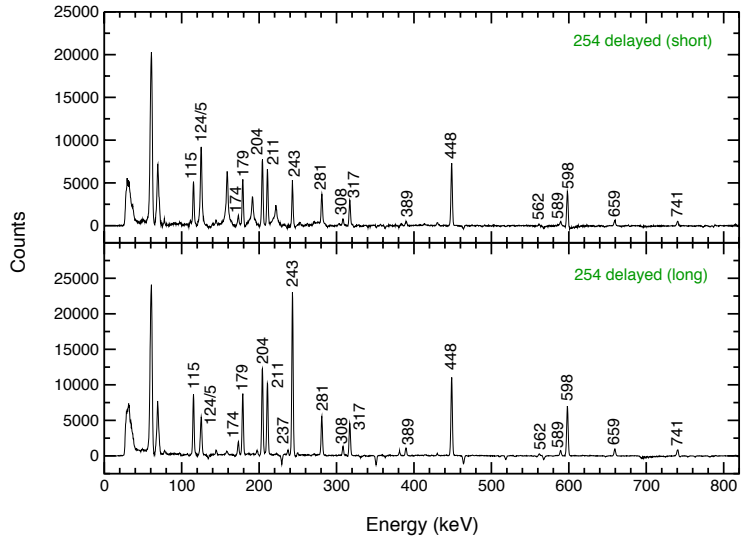

Figure 3.9: Delayed coincidence spectra gated on the 254 keV γ-ray from the early-delayed matrix.

peak (see Figure 3.12).

A gate on the 351 keV γ-ray does not show the 439, 265, and 429 keV γ-rays (see Figure 3.13) which were observed by T. Shizuma *et. al.* [15] to be transitions between the 2818 keV level and the 2124 keV level. So, it was added in parallel to the 439 keV γ-ray, and a new 88 keV γ-ray unobserved by T. Shizuma *et. al.* [15] was added due to its strong

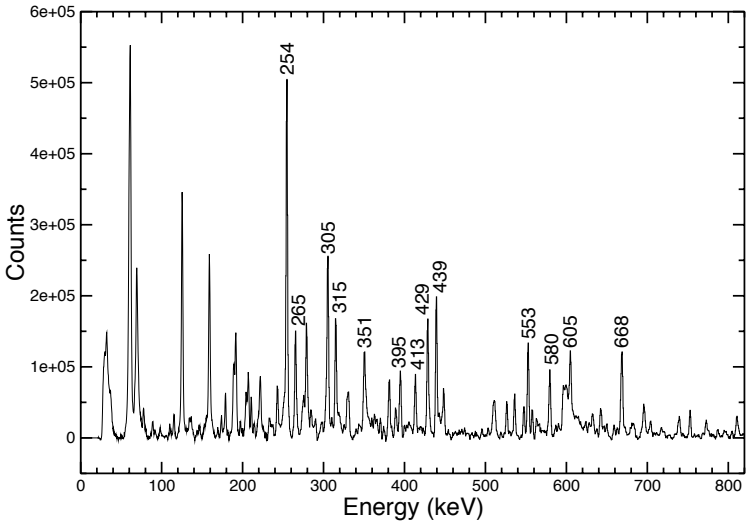

Figure 3.10: The full projection of γ-rays from the cube which preceeds the out-of-beam γ-ray gates by 30-800 ns. The numbers in the spectrum indicate the observed transitions above the isomer at 2124 keV.

intensity in the 351 keV gate and the dissapearance of the 439, 265, and 429 keV γ-rays in the 88 keV gate (see Figure 3.13).

The 88 keV gate also shows a strong 605 keV γ-ray, and the 605 keV transition was placed below the 88 keV transition because the sum of 351 and 254 is 605. This is supported by the spectrum from the early-delayed cube showing γ-rays which come later than the 605 keV γ-ray (see Figure 3.14). The peaks in this spectrum show all the γ-rays from below the isomer at the 2124 keV level.

Since a new 359 keV transition, which was not observed by Shizuma *et. al.* [15], is observed in the 605 keV gate (see Figure 3.15) with a strong intensity, it is placed above the 605 keV transition.

The sum of 351 and 89 is 395, and because the gate on the 395 keV γ-ray produces a peak at 395 keV (see Figure 3.16), it was believed that there is another transition with an energy of 395 keV.

The existence of the 207 keV transition was established by its strong intensity in the 668, 526, and 580 keV coincidence spectra (see Figure 3.17 and 3.12).

All the spectra show peaks with enegies $\sim$ 60 keV (see Figure 3.3 for their location). They are the X-rays emitted from the atomic electrons of the ^{185}Re nucleus. The X-ray energies are usually low, and have a dependence on the atomic number, Z of its parent nucleus. This confirms that the γ-ray spectra presented before show γ-rays from rhenium. The γ-rays were successfully identified as originated from ^{185}Re by setting repeated gates on known γ-rays in the ^{185}Re nucleus and seeing other known γ-rays.

There was not enough time to measure the lifetime of the intrinsic states and assign spins and parities for the new level structure deduced above the 2124 keV state. The following sections will only present the lifetime and spin/parity results for the decay scheme below this level.

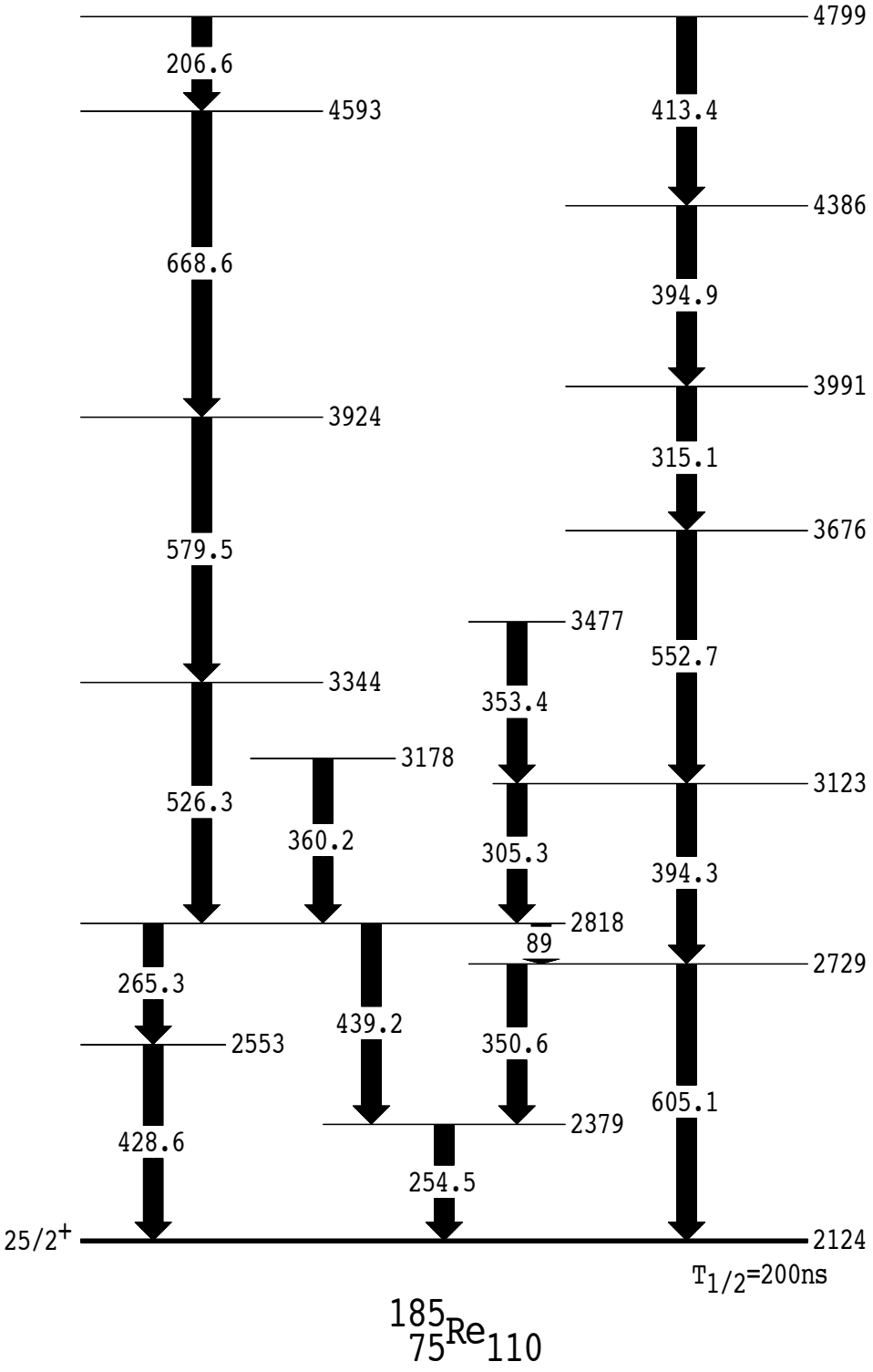

Figure 3.11: New level scheme above the 2124 keV level.

3.4 Lifetime Measurements

3.4.1 Lifetime Measurements for the 368 keV Level

The half-life for the 368 keV state in ^{185}Re was measured by M. Evans *et. al.* [37] to be 33 ± 3 ns. The half-life of this state was remeasured in the current work, and was found

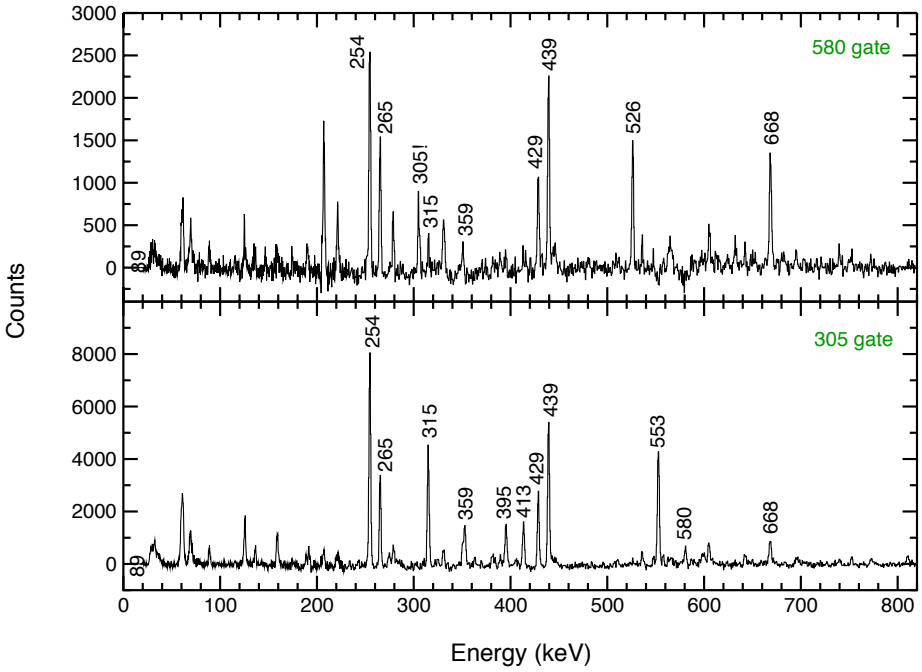

Figure 3.12: Prompt coincidence spectra gated on the 580 and 305 keV γ-rays from the cube which preceeds the out-of-beam γ-ray gates by 30-800 ns.

to be 26 ± 2 ns, determined from the relative time spectrum between the 243 and 449 keV transition (see Figure 3.18). The START and STOP indicates the direction of time. The spectrum between the 243 keV transition and the 125 keV transition shows a "time walk" due to the low energy of the 125 keV γ-ray which is intrinsically delayed as described in Section 2.6.2. Neglecting the time walk, the prompt time response curve looks like a Gaussian. The spectra which starts with the 449 keV transition and stops with the 243 keV transition shows a positive time response with a large gradient, implying that there is an isomer between them with a half-life of 26 ns. This is the half-life of the 368 keV level. Even though there are two transitions with energies of 211 keV and 179 keV between the 243 and 449 keV transitions, they are transitions within a rotational band, so are expected to have lifetimes of the order of picoseconds as mentioned in Section 1.3. This is much less than the measured 26 ns, and so can be ignored. The lifetime of the 368 keV level in ^{185}Re has not been measured since 1971 by M. Evans *et. al.* [37], and disagreement between the current measurement and the results of M. Evans *et. al.* [37] is believed to be due to their sparse data points (see Figure 3.19).

3.4.2 Lifetime measurements for the 1207 keV Level

The half-life of the 1207 keV state was measured from relative time spectra between the 204 keV transition and the 448, 659, 561, and 741 keV transitions. The relative time spectra between the 204 keV transitions and the 448 and 659 keV transitions were added. The spectrum which starts with the 204 keV transition and stops with the 449 and 659 keV transitions was overlaid on the opposite spectrum, which starts with the 449, 659 keV

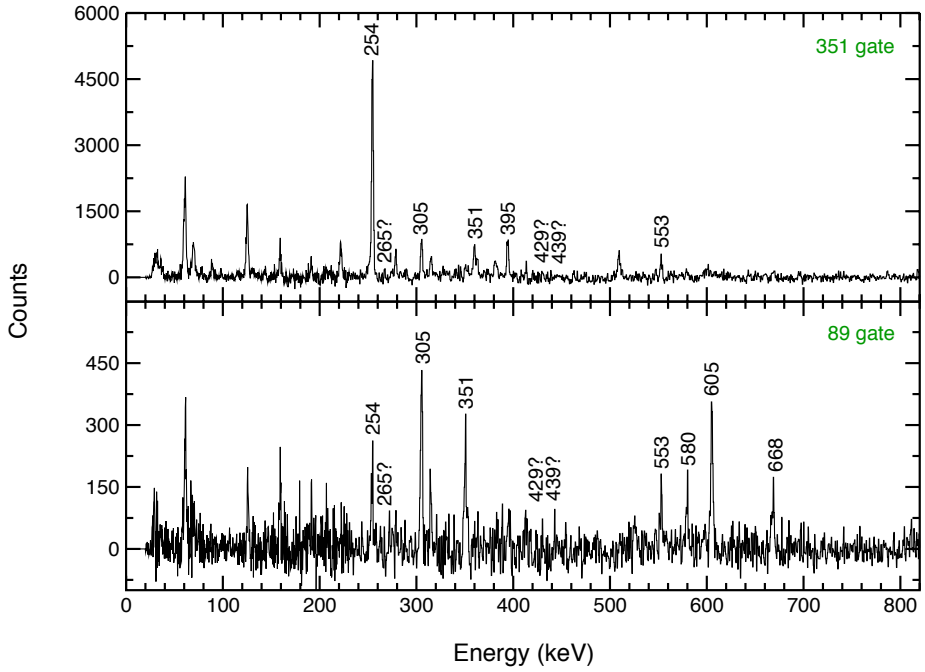

Figure 3.13: Prompt coincidence spectra gated on the 580 and 305 keV γ-rays from the cube which preceeds the out-of-beam γ-ray gates by 30-800 ns.

transitions and ends with the 204 keV transition. The relative time spectra between the 204 keV transitions and the 562 and 741 keV transitions were added to investigate the lifetime of the 1109 keV level. The spectrum which starts with the 204 keV transition and stops with the 562 and 741 keV transitions was overlaid on the opposite spectrum, which starts with the 562, 741 keV transitions and ends with the 204 keV transition. The shift in centroid is consistent with the previous spectrum, and therefore rules out the possibility that the 1109 keV state is an isomer (see Figure 3.20). The half-life of the 1207 keV state was measured from the centroid shifts of these two spectra, and found to be 1.3 ± 0.6 ns. This value is inconsistent with 6 ± 2 ns measured by T. Shizuma *et. al.* [15].

3.4.3 Lifetime Measurements for the state between the 1207 keV and 1411 keV Level

The relative time spectra which start with the 281, 308, 317, 589, 598 keV transitions and stop with the 204 keV transition were added and overlaid on the relative time spectrum which are the addition of the spectra which start with the 281, 308, 317, 589, 598 keV transitions and stop with the 173 keV transition. There would be a difference between them if the state between the 1207 keV and 1411 keV level is at 1380 keV, and has a lifetime. However, no difference between the spectra was observed (see panel (a) of Figure 3.21). If the state between the 1207 keV and 1411 keV level is at 1238 keV, there should be a difference between the relative time spectrum which starts with the 204 keV transition and ends with the 448 keV transition, and the relative time spectrum which starts with the 173 keV transition and ends with the 448 keV transition. Again, they do

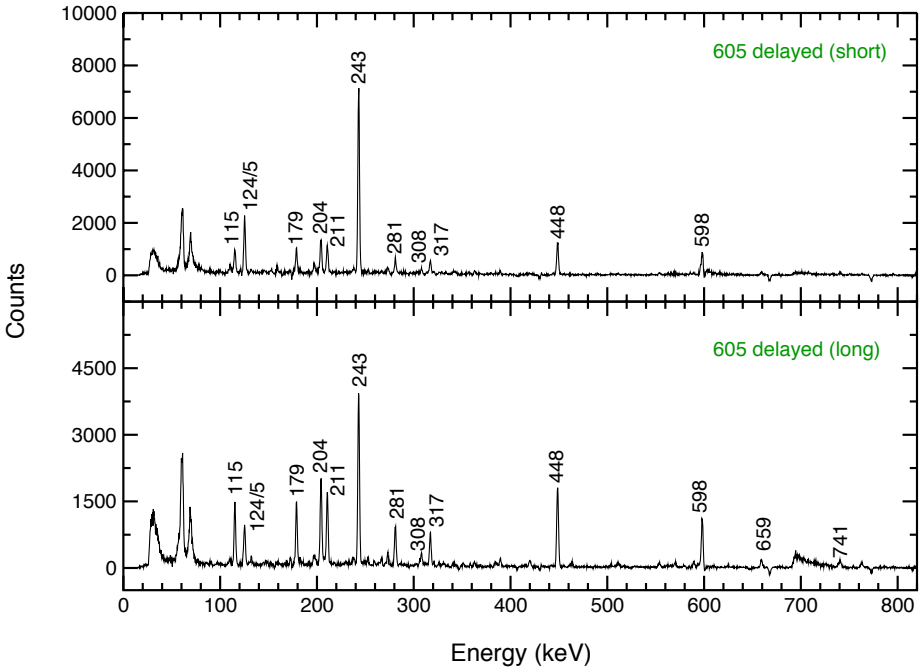

Figure 3.14: Prompt coincidence spectra gated on the 351 and 88 keV γ-rays from the cube which preceeds the out-of-beam γ-ray pairs by 30-800 ns.

not show any difference (see panel (b) of Figure 3.21). This shows that the state between the 1410 and 1206 keV level is not an isomer. Unfortunately, this means that we cannot order the 31 keV transition and the 173 keV transition. However, since the 1411 keV level is an isomer, there is a high possibility that the 1411 keV level will decay via a very low energy transition. Therefore, the 31 keV transition was placed above the 173 keV transition.

3.4.4 Lifetime Measurements for the 1411 keV Level

The 1411 keV state in ^{185}Re had not been identified as an isomer previously [15]. However the half-life of this state has been measured here to have a significant value of 5.5 ± 1.4 ns. The time spectra used to obtain this figure is shown in Figure 3.22. This lifetime was measured from a relative time spectrum which was a result of adding the spectra which start with the 281, 308, 317, 589, 598 keV transitions and stop with the 204 keV transition (see panel (a) of Figure 3.22).

If we sum the measured half-lives of the 1207 and 1411 keV isomer, we obtain a value which agrees with 6 ± 2 ns measured by T. Shizuma and co-workers [15] for the half-life of the 1207 keV level. It is believed that what they have actually measured is the total half-life of the 1207 and 1411 keV levels since their result is based on the relative time spectra between the 204, 281, 598 and 448 keV transitions (see Figure 3.25).

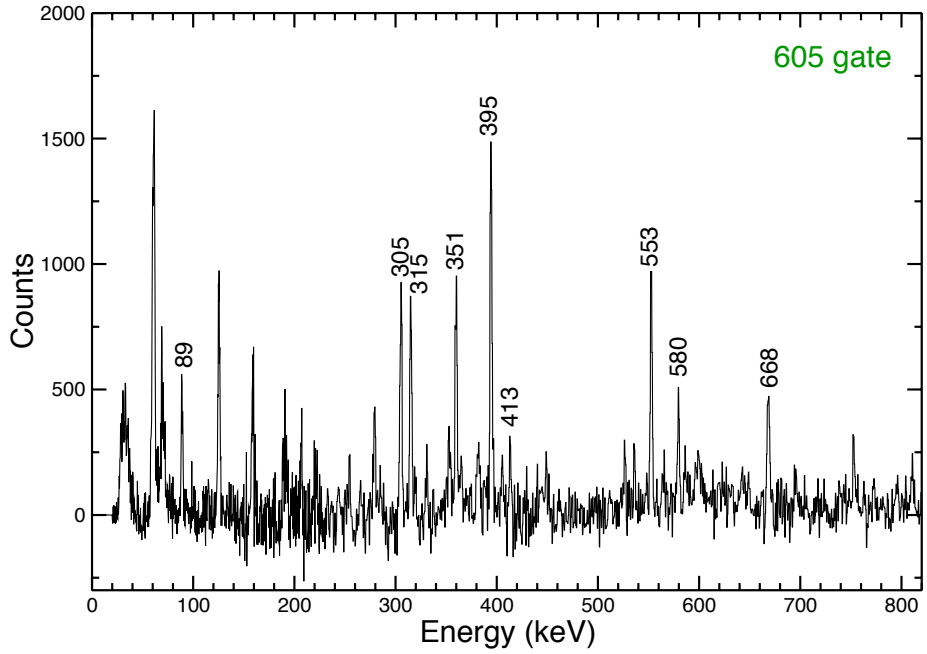

Figure 3.15: Delayed coincidence spectra gated on the 605 keV γ-ray from the early-delayed matrix.

3.4.5 Lifetime Measurements for the 2009 keV Level

The relative time spectrum which starts with the 115 keV transition and stops with the 598 keV transition is overlayed onto the spectrum which starts with the 598 keV transition and stops with the 115 keV transition. There was no detectable centroid shift in that spectrum, implying that there is no lifetime for the 2009 keV level (see panel (b) of Figure 3.22).

3.4.6 Lifetime measurements for the 2124 keV Level

The lifetime of the long lived isomer in ^{185}Re at 2124 keV has been remeasured. The intensity of six γ-rays immediately below the isomer have been measured in six different time bins, $\sim$ 111.5 nanoseconds apart between beam pulses (see Figure 3.23). The graphs of ln (I) against t for these γ-rays are shown in Figure 3.24.

The measured half-lives for the 2124 keV state from the graphs in Figure 3.24 are shown in Table 3.2.

The half-life for the 2124 keV state was not measured from the decay in intensity of transitions below the 1410 keV state. Since that state is also an isomer, the decay in intensity of those γ-rays is not directly related to the meanlife of the 2124 keV state by the exponential decay law described by equation 2.1.

The mean value of the six different measured half-lives was calculated to be 200.6 ns. The error was estimated as half the range of the measured values, which is 3.4 ns. This was rounded to 200 ± 4 ns. This value does not agree with the half-life of 123 ± 23 ns, previously measured by T. Shizuma and co-workers [15]. However, the results presented in

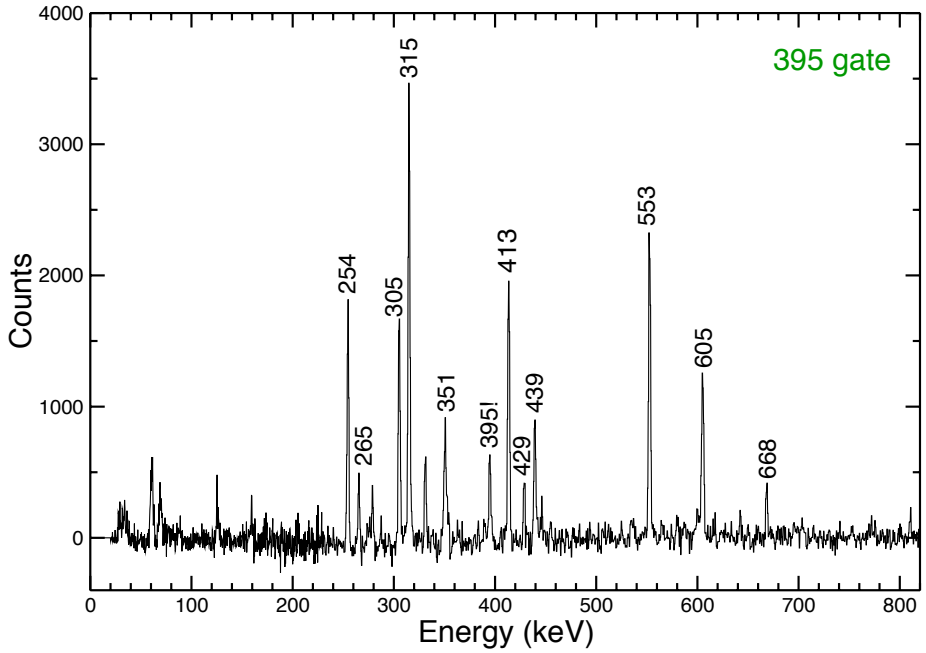

Figure 3.16: Prompt coincidence spectrum gated on the 395 keV γ-ray from the cube which preceeds the out-of-beam γ-ray pairs by 30-800 ns.

E_γ (keV)	$T_{1/2}$ (ns)
115.2	196.4
281.0	202.1
308.3	199.3
317.1	200.4
589.3	203.1
598.2	202.4

Table 3.2: Half-life of the 2124 keV state measured from the intensity reduction of the 115, 281, 308, 317, 589 and 598 keV transitions between beam pulses.

this thesis are not believed to be inconsistent with their measurement. Their data points for measurement of the half-life for the 2124 keV state are shown in Figure 3.25 as open triangles measured from between the 254, 305 and 439 keV and the 115, 204 and 598 keV transitions. It is feasible for a line of best fit corresponding to a half-life of 200 ns to be drawn through those points.

3.5 Spin and Parity Assignments below the 2124 keV State

The spins and parities for states in ^{185}Re were not well determined by T. Shizuma *et. al.* [15] above the 1207 keV state. However, the spins and parities for states between 1207 and 2124 keV in energy have been determined in the present work.

The angular correlation curves across the isomer at 368 keV will be attenuated due

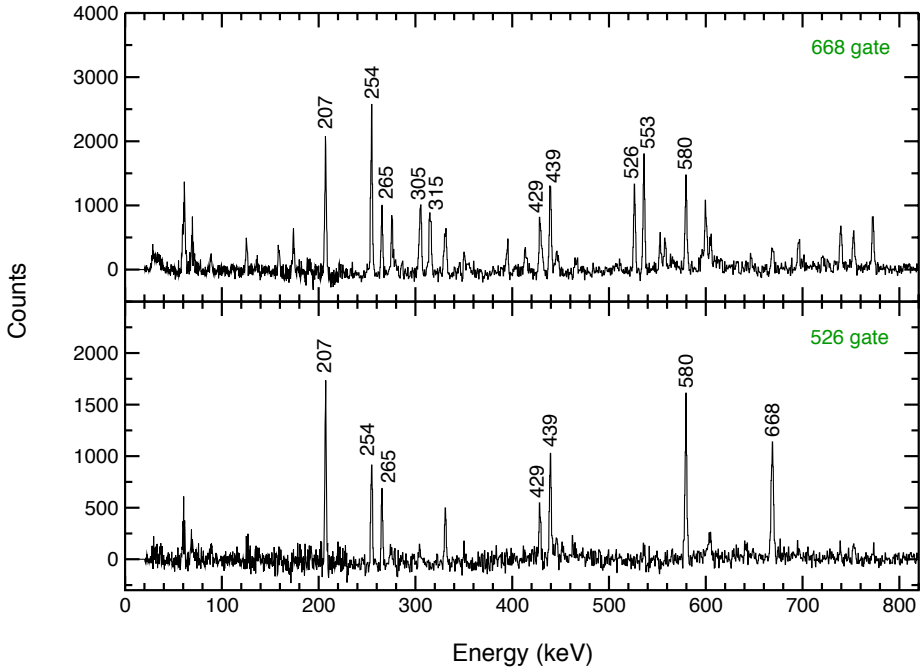

Figure 3.17: Prompt coincidence spectra gated on the 668 and 526 keV γ-rays from the cube which preceeds the out-of-beam γ-ray pairs by 30-800 ns.

its long lifetime, so the experimental data points for the transitions between the 368 keV level and 1206 keV level were analysed first. The 9/2-[514] rotational band in ^{185}Re is well known previously [37], therefore the 390 keV transition with $\Delta J = 2$ within the band was assumed to be an E2 transition, based on the rotational model described in Section 1.4. The angular correlation curve between the 390 keV transition and 449 keV transition effectively removes the contribution from the in-band $\Delta J = 2$, 448 keV transition from the 996 keV level to the 548 keV level (see Figure 3.2). So, the experimental data points for the angular correlation between the 390 and the 449 transitions shown in the top left panel of Figure 3.26, is the angular correlation between the 390 keV transition from the 758 keV level to the 368 keV level and the 449 keV transition from the 1207 keV level to the 758 keV level. Also in that panel, the theoretical curve for the angular correlation between an E2 transition and a mixed M1/E2 transition with a mixing ratio, $\delta = 0.6$ is overlaid on the experimental data. The theoretical curve fits the experimental data points with reasonable accuracy, so it was concluded that the 449 keV transition from the 1207 keV level to the 758 keV level is a mixed M1/E2 with a mixing ratio of approximately 0.6. With the multipolarity of the 449 keV transition from the 1207 keV level to the 758 keV level known, the multipolarity of the 211 keV transition from the 758 keV level to the 548 keV level can be determined. The intensity of the 211 keV transition from the 1207 keV level to the 996 keV level is much less than the intensity of the 211 keV transition from the 758 keV level to the 548 keV level, and the 448 keV transition from the 996 keV level to the 548 keV level is much less in intensity than the 449 keV transition from the 1207 keV level to the 758 keV level (see Table 3.1). So, the experimental data points for the angular

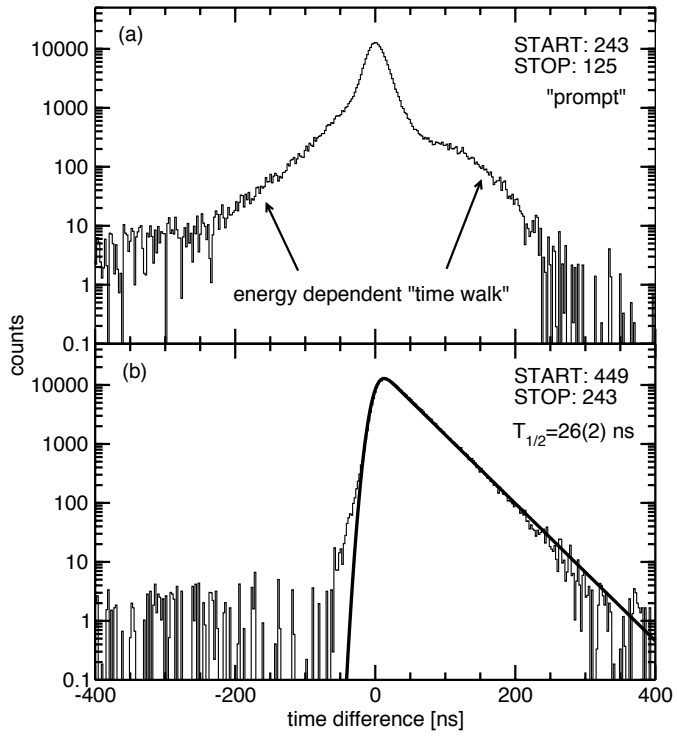

Figure 3.18: Relative time spectra for the 125/243 and 449/243 keV γ-rays. (a) The prompt spectrum between the 125 and 243 keV transitions does not show a measurable lifetime. (b) There is a measurable lifetime in the 449/243 relative time spectrum, implying the presence of a $T_{1/2} = 26$ ns isomer at 368 keV. The direction of the lifetime implies that the 243 keV transition is after the 449 keV transition.

correlation between transitions with energies 211 keV and 449 keV should corespond to the 211 keV transition from the 758 keV level to the 548 keV level and the 449 keV transition from the 1207 keV level to the 758 keV level respectively. A subsequent theoretical fit performed on the experimental data points for the angular correlation between the 449 keV transition and the 211 keV transition revealed that the 211 keV transition from the 758 keV level to the 548 keV level is a mixed M1/E2 transition with mixing ratio, $\delta = 0.2$ (see top right panel of Figure 3.26). The data points for the angular correlation between the 211 keV transition and the 179 keV transition in the $9/2^-[514]$ band agrees with a theoretical angular correlation between a mixed M1/E2 transition and another mixed M1/E2 transition, both with a mixing ratio, $\delta = 0.2$ (see middle left panel of Figure 3.26).

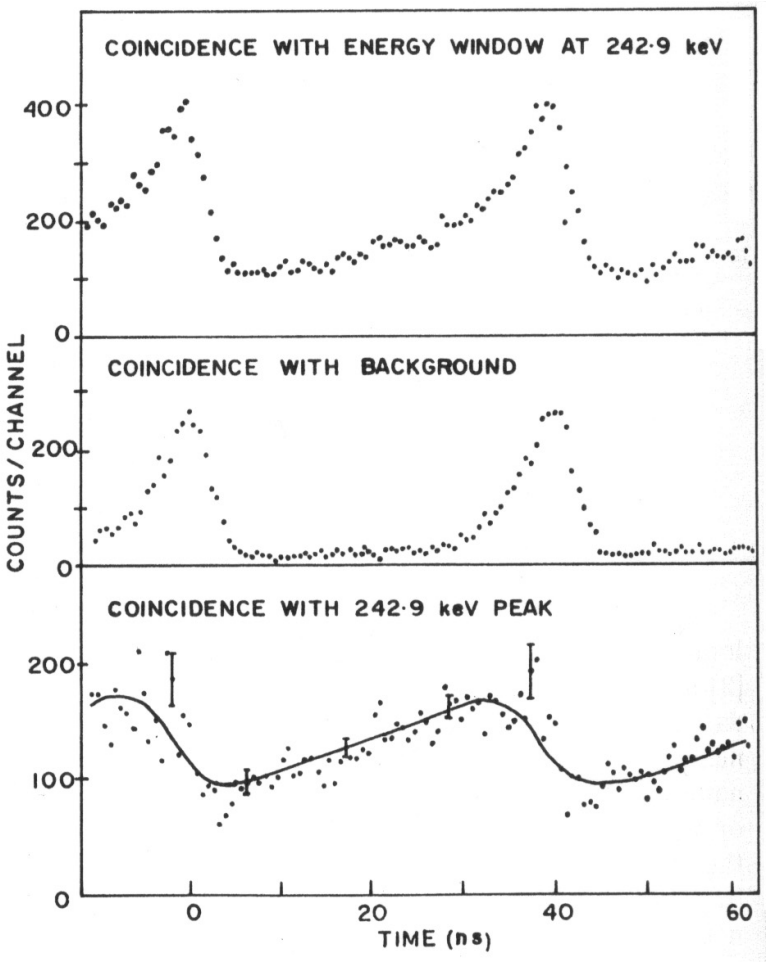

Figure 3.19: The data points used by M. Evans *et. al.* [37] to measure the half-life of the 368 keV state has a huge spread.

3.5.1 Spin and Parity Asignments for the 1109, 1207 and 1411 keV Levels

The multipolarity of the 179 keV transition from the 548 keV level to the 368 keV level is now known, and the spin and parity of the 1109 keV level previously unobserved by T. Shizuma *et. al.* [15] and the 1207 level, which was not definitively assigned a spin and parity in their publication can be determined. The experimental data points for the angular correlation between the 179 keV transition and the 659 keV transition from the 1207 keV level to the 548 keV level agrees with the theoretical curve between an M1/E2 transition and an E2 transition (see middle right panel of Figure 3.26). Therefore, the 1207 keV level was assigned a spin and parity of $15/2^-$. However, as can be seen from the theoretical fit in the middle left and right panel in Figure 3.26, the theoretical angular correlation curve between a mixed M1/E2 transition and another mixed M1/E2 transition is similar to the correlation between a mixed M1/E2 transition and a pure E2 transition. If the 659 keV transition is a mixed M1/E2 transition, the spin and parity of the 1207 keV level will be $13/2^-$. This will still be consistent with a mixed M1/E2 multipolarity for the 449 keV transition from the 1207 keV level to the 758 keV level. As will be discussed in the next chapter, this ambiguity can be resolved by looking at the reduced hindrances for decays out of the 1207 keV state, and the spin and parity for the 1207 keV level was

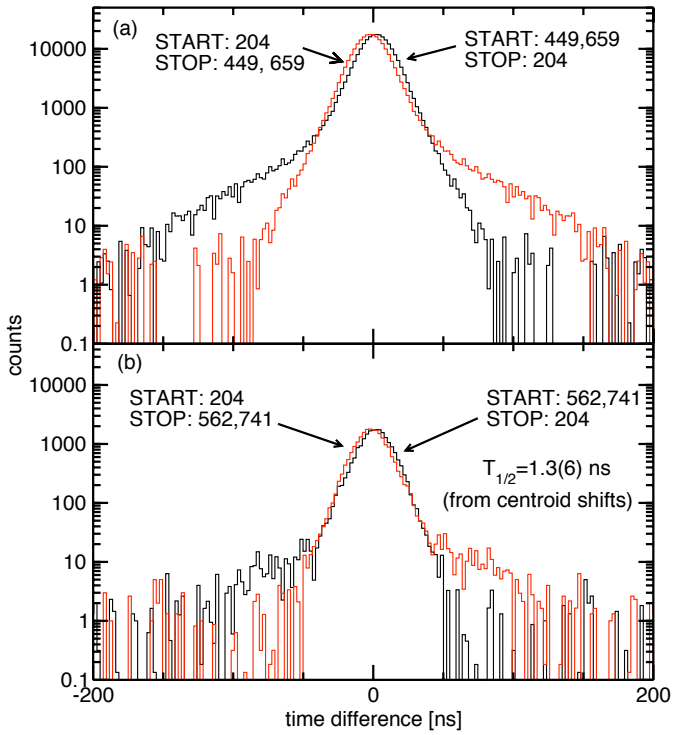

Figure 3.20: Relative time spectra showing the lifetime measurement of the 1207 keV level from centroid shifts. (a) Spectrum between the 204 and the 449 and 659 keV γ-rays. (b) Spectrum between the 204 and the 562 and 741 keV γ-rays. There is no difference between them, so the 1108 keV state is not an isomer. The shifts are small, but the direction of shift is consistent with $T_{1/2} = 1.3$ ns in each case.

assigned as $15/2^-$.

The multipolarity for the transitions above the isomer at 368 keV was deduced, and even though the angular correlation curves between the transitions below and above the isomer is attenuated, this effect is not large as can be seen in the theoretical fits to the experimental data between the 243 keV transition and the 179 keV transiton. The experimental data points for the correlation between the 243 keV transition and the 179 keV transition agrees with the theoretical correlation between an E1 transition and a mixed M1/E2 transition with a mixing ratio of 0.2 (see bottom right panel of Figure 3.26). Since the 243 keV transition has a known multipolarity of E1, the experimental data points for the angular correlation between the 243 keV transition and the transitions above the 368 keV isomer could be trusted. The experimental data points for the angular correlation between the 243 keV transition and the 741 keV transition agrees with the theoretical curve for a correlation between an E1 transition and an E2 transition (see bottom left

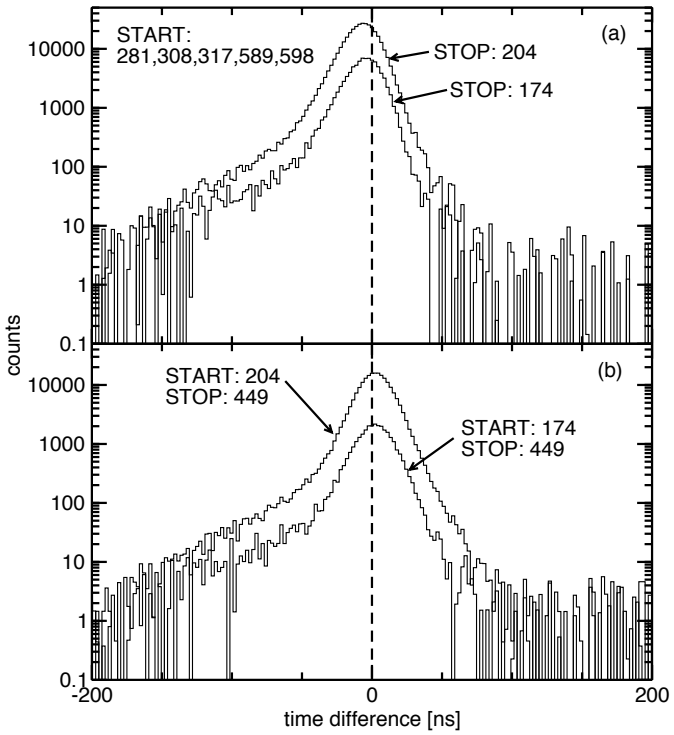

Figure 3.21: Relative time spectra showing no measurable lifetime for the state between the 1410 and 1206 keV level .(a) Relative time spectra the 204 keV and 174 keV γ-ray with earlier transitions. (b) Relative time spectra the 204 keV and 174 keV γ-ray with later transitions.

panel of Figure 3.26). Therefore, the 741 keV transition could be an E2 transition, so the spin and parity of the 1109 keV level previously unobserved by T. Shizuma *et. al.* [15] is temporarily assigned as $13/2^-$.

To confirm the spin and parity of the 1109 keV state, the theoretical fits to the experimental data points for the angular correlation between the 204 keV transition and the 659 keV, 449 keV transitions were used to deduce the multipolarity of the 204 keV transition. The angular correlation between the 204 keV transition and the 449 keV transition was expected to isolate the 448 keV in-band transition from the 996 keV level to the 548 keV level, since this transition is extremely weak relative to the 449 keV transition from the 1207 keV level to the 758 keV level. The multipolarities of the 659 keV and the 449 keV transition were deduced previously as E2 and M1/E2 with $\delta = 0.6$ respectively. The experimental data points for the angular correlation between the 204 keV transition and the 659 keV transition agree with a theoretical curve for the angular correlation between an E2 and another E2 transition, and the experimental data points for the angular correlation between the 204 keV transition and the 449 keV transition agrees with a theoretical

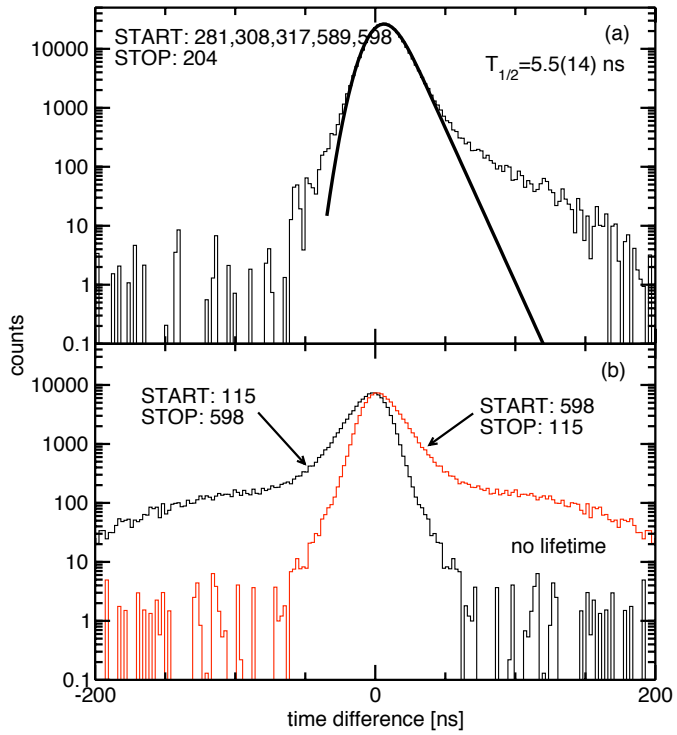

Figure 3.22: Relative time spectra for measuring the lifetimes of the 1410 and 2009 keV level. (a) The relative time spectrum between the 281, 308, 317, 589, 598 and the 204 keV transition shows a half-life of 5.5 ns. (b) There is no measurable lifetime in the 115/598 and the 598/115 relative time spectra.

curve for the angular correlation between an E2 transition and a mixed M1/E2 transition with mixing ratio, δ=0.6, so the multipolarity of the 204 keV transition was deduced to be E2 (see top left and middle left panel of Figure 3.27). This means that the spin and parity of the 1411 keV level is $19/2^-$. A further theoretical fit to the data points for the angular correlation between the 204 keV transition and the 741 keV transition confirms that the 741 keV transition is an E2 transition (see top right panel of Figure 3.27), as suggested before from the angular correlation between the 243 keV transition and the 741 keV transition. Therefore, the 1109 keV level was confidently assigned a spin and parity of $13/2^-$.

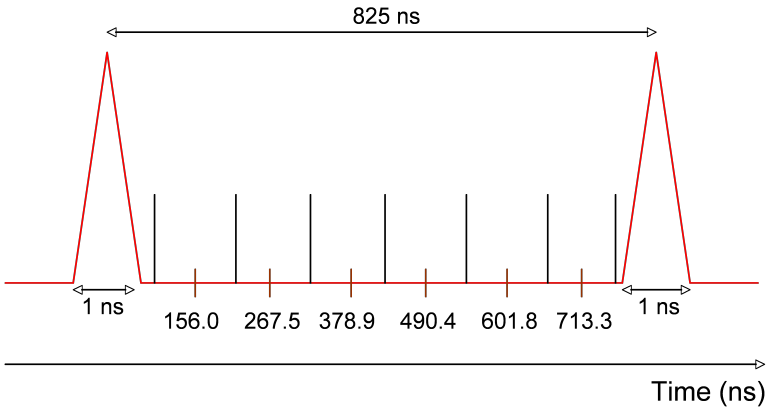

Figure 3.23: The intensities of six γ-rays immediately below the isomer at 2124 keV were measured in six different time bins, $\sim$ 111.5 nanoseconds apart between beam pulses, as illustrated here.

3.5.2 Spin and Parity Assignments for the 1692, 2000 and 2009 keV Levels

The experimental data points between the 204 keV transition and the 281 keV transition agrees with the theoretical angular correlation curve between an E2 and a mixed M1/E2 transition with a mixing ratio, $\delta = 0.7$ (see middle right panel of Figure 3.27). Thus, the 281 keV transition was deduced to have a mixed multipolarity of M1/E2 with a mixing ratio of 0.7 since the 204 keV transition is now a known E2 transition. This leads to the assignment of a spin and parity of $21/2^-$ for the 1692 keV level. The experimental data points for the angular correlation between the 204 keV transition and the 589, 598 keV transitions agree with the theoretical curves for a correlation between an E2 transition and another E2 transition (see bottom left and bottom right panel of Figure 3.27). Therefore, both the multipolarities of the 589 and 598 keV transitions were deduced to be E2. The spin and parities of the 2000 keV level and the 2009 keV level were assigned as $23/2^-$ based on this information.

3.5.3 Spin and Parity Assignments for the 2124 keV Level and the Level Between 1207 and 1411 keV

The experimental data points for the angular correlations between the 173 keV transition and the 589, 598 transitions (known to be E2 transitions from Section 3.5.2) agree with a theoretical angular correlation curve between an M1 and an E2 transition (see top left and top right panel of Figure 3.28). Also, the experimental data points for the angular correlation between the 173 keV transition and the 281 keV transition (known to be a mixed M1/E2 transition with $\delta = 0.7$ from Section 3.5.2) agrees with the theoretical angular correlation curve between an M1 and a mixed M1/E2 transition with a mixing ratio of 0.7 (see middle left panel of Figure 3.28). Thus, the multipolarity of the 173 keV transition was deduced to be an M1 transition. This would mean that the spin and parity of the state between the 1207 keV level and the 1411 keV level is $17/2^-$, regardless of the order of the 31 keV transition and the 173 keV transition. Unfortunately, this will mean that the energy of the new state between the 1207 and the 1411 keV level not observed by T. Shizuma *et. al.* [15] cannot be determined. However, the 31 keV transition is a very low energy transition, so it is speculated that it might depopulate an isomer, giving an

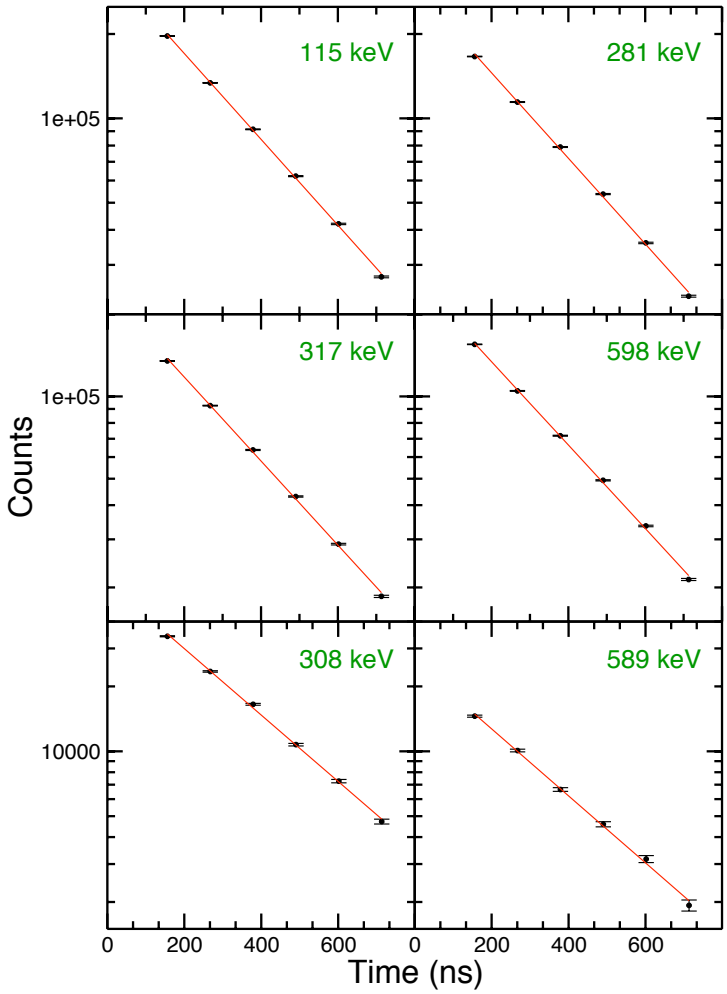

Figure 3.24: Graphs of ln (I) against t for the 115, 281, 308, 317, 589 and 599 keV γ-rays and the fitted lifetimes. The measured half-lives for each individual graphs are shown in Table 3.2. The final value for the half-life of the 2124 keV level was measured to be 200 ± 4 ns.

energy of 1380 keV to the newly discovered state between the 1207 keV and the 1411 keV level.

The experimental data points for the angular correlation between the 115 keV and the 598 keV transition (known E2 transition from Sectionac2) agrees with the theoretical angular correlation curve between an E1 transition and an E2 transition (see middle right of Figure 3.28). Furthermore, the experimental data points for the angular correlations between the 115 keV transition and the 281 keV transition (known to be a mixed M1/E2 with $\delta = 0.7$) agrees with the theoretical angular correlation curve between an E1 and a mixed M1/E2 transition with a mixing ratio of 0.7. Therefore, the multipolarity of the 115 keV transition out of the isomer at 2124 keV was deduced as E1. This follows the assignment of $25/2^+$ for the spin and parity of the 2124 keV level. The experimental data points for the angular correlation between the 317 keV transition and the 281 keV transition agrees with the theoretical angular correlation curve between an mixed M1/E2 transition with $\delta = 0.7$ and another mixed M1/E2 transition with the same mixing ratio. This suggest that the 317 keV transition has a multipolarity of M1/E2 with mixing ratio of 0.7. This is consistent with the spin and parity assignment of $23/2^-$ for the 2009 keV

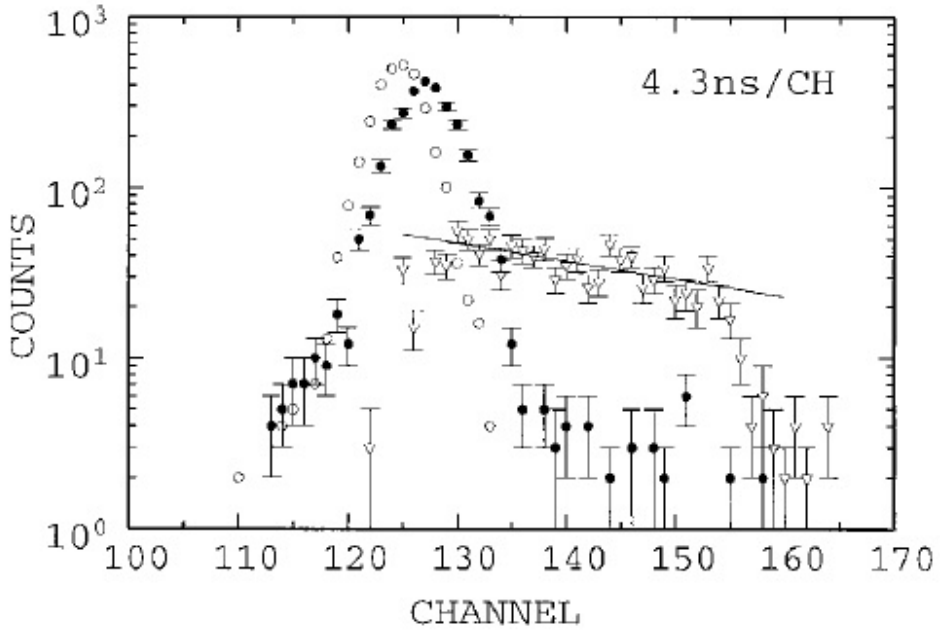

Figure 3.25: The relative time spectra between the 448 and the 204, 281, and 598 keV transitions are indicated by filled circles, believed by T.Shizuma *et. al.* to show the lifetime of the 1207 keV level. They measured the half-life of the 2124 keV state using the spectra between the 254, 305, 439 and the 115, 204, 598 keV transitions (open triangles). A line of best fit showing a half-life of 200 ns could be drawn through these points. Diagram extracted from T. Shizuma *et. al.* [15]

level and $21/2^-$ for the 1692 keV level.

The mixing ratios for the mixed M1/E2 transitions mentioned above are only approximate values. The value for the mixing ratios and their uncertainties can be more properly obtained by means of a χ^2 minimisation analysis for the angular correlations between transitions in the case where at least one of the transition is mixed [25]. Unfortunately, time constraints did not allow such analyses to be performed in the current work.

3.6 Branching Ratios

The branching ratios (λ) between the $\Delta J = 2$ transition and $\Delta J = 1$ transitions in the $K^\pi = 9/2^-$ and $K^\pi = 19/2^-$ rotational band in the ^{185}Re nucleus were measured. They were obtained from the following:

$$\lambda = \frac{I_\gamma(\Delta J = 2)}{I_\gamma(\Delta J = 1)} \tag{3.1}$$

where I_γ intensity of the γ-ray measured from equation 2.4. The measured branching ratios are shown in Table 3.3.

3.7 Intensity Balance - E1 Assignment for the 115.2 keV Transition

In an out-of-beam spectrum gated by the 281.0 keV transition, it is possible to perform a total intensity balance between the 115.2 and 317.1 keV transitions, using equations 2.4

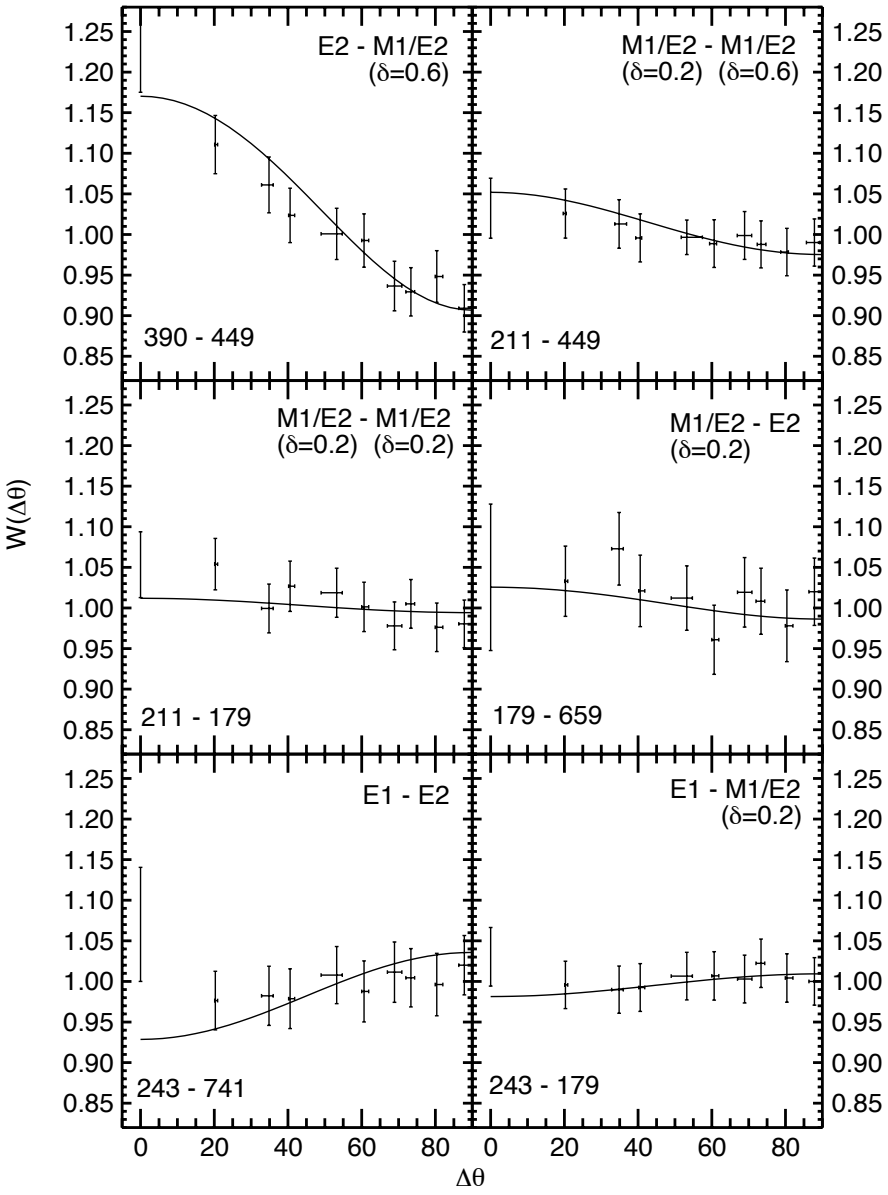

Figure 3.26: Theoretical angular correlations fitted against experimental data points to deduce the spin and parity for the 1109, 1207 and 1411 keV levels.

K^π	Level (keV)	$E_\gamma(\Delta J = 2)$ (keV)	$E_\gamma(\Delta J = 1)$ (keV)	λ
$9/2^-$	758	389.1	210.7	0.133 (6)
$9/2^-$	996	448.2	237.5	0.300 (13)
$19/2^-$	2000	589.3	308.3	0.647 (96)

Table 3.3: Branching ratios for the 758, 996 keV states in the $K = 9/2$ band, and 2000 keV state in the $K = 19/2$ band.

and 2.5. Such a balance gives $\alpha_T = 0.16 \pm 0.18$ for the 115.2 keV transition. Theoretical values of the conversion coefficient would be 0.266 (E1), 3.45 (M1), 2.36 (M2) and higher values for higher multipolarities. Clearly the 115.2 keV transition must have E1

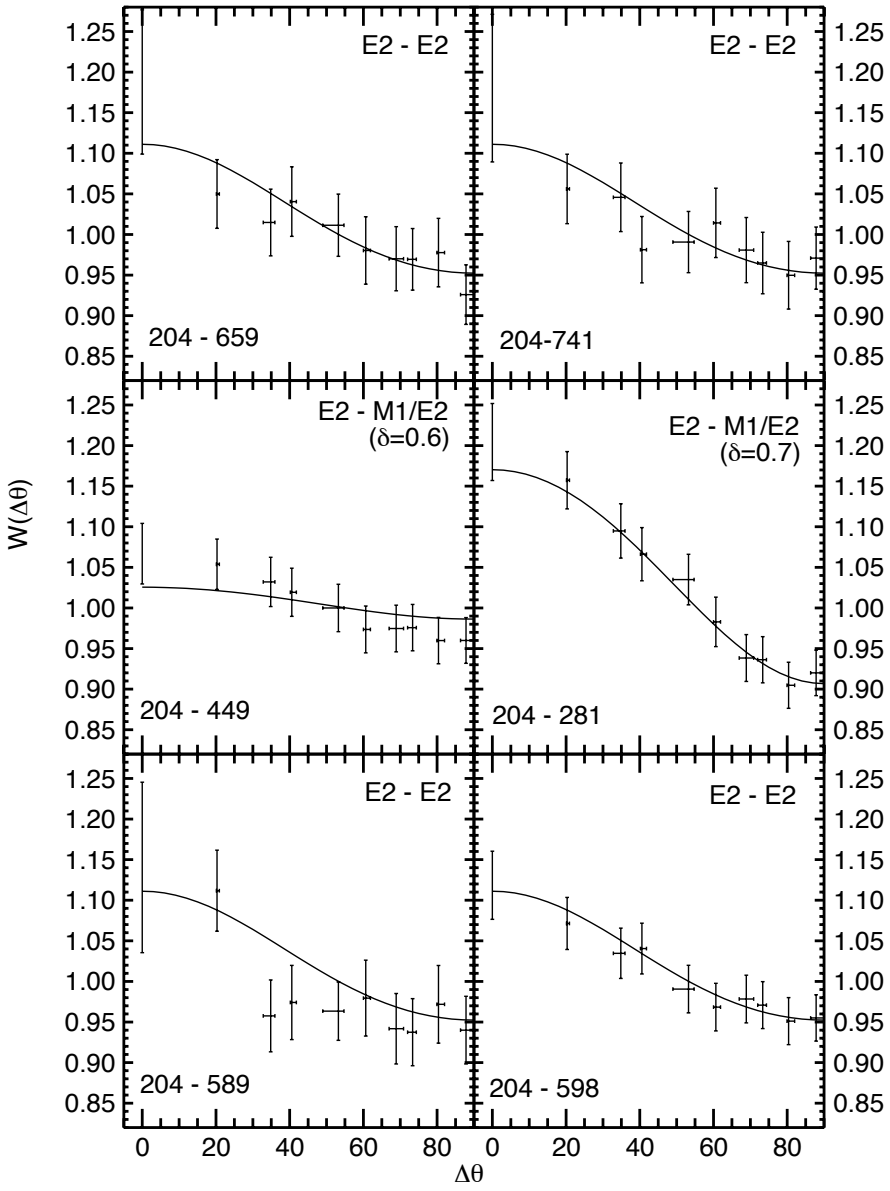

Figure 3.27: Theoretical angular correlations fitted against experimental data points to deduce the spin and parity for the 1692, 2000 and 2009 keV levels.

multipolarity.

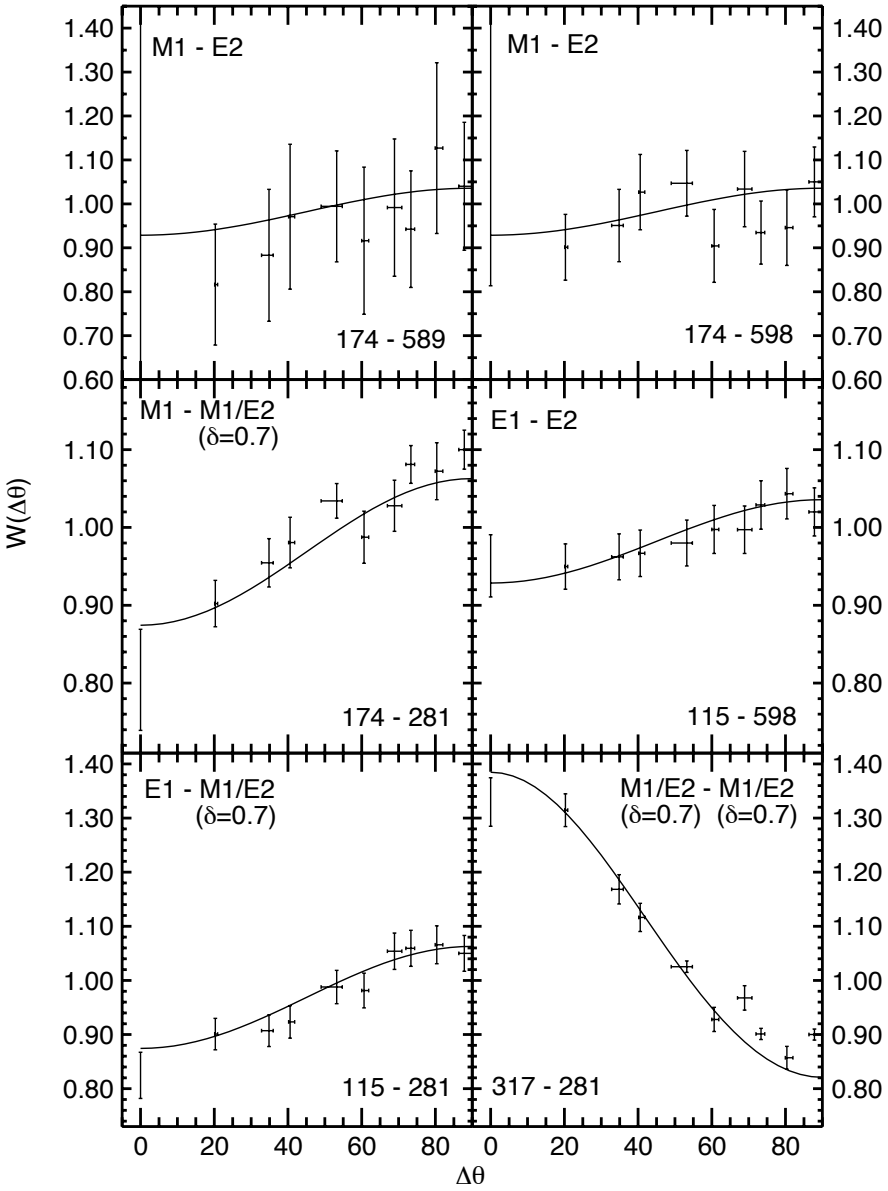

Figure 3.28: Theoretical angular correlations fitted against experimental data points to deduce the spin and parity for the 2124 keV level and the level between 1207 and 1411 keV

Chapter 4

Discussion

This chapter consists of the consideration of the reduced hindrances out of the 1207 keV level to determine its spin and parity. Then, the magnetic properties for the rotational bands in ^{185}Re are discussed. Finally, the results of multi-quasiparticle calculations for ^{185}Re is presented, and compared with the level scheme obtained experimentally.

4.1 Spin and Parity for the 1207 keV State

As mentioned in Section 3.5.1, there is an ambiguity in deducing the spin and parity of the 1207 keV state from angular correlations. Therefore, the spin and parity of the 1207 keV level was deduced from the reduced hindrance factor f_ν, of the transitions out of this state. As described in Section 1.3, the value of f_ν should be approximately 100.

The lowest state which the 1207 keV state decays to is the first rotational state of the $9/2^-[514]$ intrinsic Nilsson state with spin and parity $11/2^-$, and the highest is a state with spin and parity $15/2^-$ in the same rotational band. The value of the reduced hindrance factor, f_ν was determined from equation 1.11 for the possibilities that the 1207 keV state has a spin of 13/2, 15/2 and 17/2. The results are presented in Table 4.1. These possible spins correspond to the multipole order of the transitions out of the 1207 keV state of not more than 3, since higher multipolarity will be extremely unlikely (see equations 1.4, 1.5 and 1.8).

The only J^π assignment which gives a value of $f_\nu \sim 100$ for all the transitions out of the 1206 keV state is $15/2^-$, so it was concluded that the 1206 keV state has a spin and parity of $15/2^-$.

4.2 Magnetic Properties of Rotational Bands in Odd-mass Rhenium Nuclei

As mentioned in Section 1.4 in Chapter 1, the mixing ratio δ, for the mixed M1/E2 transition in a rotational band and the magnetic moment of the nucleus (related to $|g_K - g_R|$) can be measured experimentally from the known branching ratio, λ between the $\Delta J = 1$ and the $\Delta J = 2$ in-band transitions, the quadrupole moment of the nucleus, Q_0 and the transition energies in the rotational band.

Three single particle states with associated rotational band members have been observed for ^{185}Re in the current work, the $5/2^+[402]$ band, the $9/2^-[514]$ band, and the newly discovered band with $K^\pi = 19/2^-$ (previously unobserved by T. Shizuma *et. al.* [15]). The $5/2^+[402]$ and the $9/2^-[514]$ bands were observed in other odd-mass rhenium nuclei; ^{181}Re [39] and ^{183}Re [40]. The $|g_K - g_R|$ values and mixing ratios deduced from the

J^π	E_γ (keV)	$T\lambda$	f_ν
$13/2^-$	211.0	M1	1.47×10^4
	448.7	M1	7638
	659.4	M1	1.94×10^5
	97.8	M1	4456
$13/2^+$	211.0	E1	1.34×10^6
	448.7	E1	6.95×10^5
	659.4	E1	1.76×10^7
	97.8	E1	4.06×10^5
$15/2^-$	211.0	M1	121
	448.7	M1	87
	659.4	E2	205
	97.8	M1	67
$15/2^+$	211.0	E1	1162
	448.7	E1	837
	659.4	M2	1.68
	97.8	E1	639
$17/2^-$	211.0	M1	24
	448.7	E2	1.9
	659.4	M3	3.79×10^{-7}
	97.8	E2	3687
$17/2^+$	211.0	E1	137
	448.7	M2	0.24
	659.4	E3	2.25×10^{-3}
	97.8	M2	0.04

Table 4.1: Reduced hindrance factor (f_ν) calculated for different possible spin and parity assignments (J^π) for the 1206 keV state, assuming pure multipolarities for the decays.

in-band branching ratios for the transitions in the $K^\pi = 9/2^-$ band for ^{185}Re were measured, and compared to those measured in ^{181}Re and ^{183}Re, and presented in Table 4.2. The quadrupole moment, Q_0, for ^{185}Re was assumed to be the same as ^{183}Re [41]. The spin and parity of the initial state, in which the nucleus can decay via a mixed M1/E2 transition or an E2 transition, is denoted by J^π. The value for $|g_K - g_R|$ and δ for the M1/E2 transitions in the $K^\pi = 9/2^-$ band agree with those in ^{181}Re and ^{183}Re, indicating a consistent behaviour for the $K^\pi = 9/2^-$ band across odd-mass rhenium isotopes with atomic masses 181, 183, and 185. Nevertheless, more measurements should be performed on transitions higher up the band in ^{185}Re to confirm this behaviour. There was not enough time to measure the mixing ratios for the mixed M1/E2 transitions in the $K^\pi = 5/2^+$ band for ^{185}Re, so a comparison could not be made to the $K^\pi = 5/2^+$ bands in ^{181}Re and ^{183}Re.

The $K^\pi = 9/2^-$ state corresponds to a single particle in the $9/2^-[514]$ Nilsson state. The g_K value for this particle was calculated assuming a deformation parameter of $\epsilon_2 = 0.217$ [14] and a g_R value of 0.3 [13] was used for the ^{185}Re nucleus. The calculated $g_K - g_R$ value is 1, which is in good agreement wih the experimental value of 0.972. The $K^\pi = 19/2^-$ was deduced to be a three quasi-particle state, with two neutrons in the $3/2^-[512]$ and the $11/2^+[615]$ Nilsson states, and one proton in the $5/2^+[402]$ Nilsson state. The calculated $g_K - g_R$ value for this configuration is 0.09, in reasonable agreement with the experimental value of 0.198 ± 0.024. Therefore, the $K^\pi = 19/2$ state is believed

Nucleus	$E_\gamma(\Delta I=1)$ (keV)	$E_\gamma(\Delta I=2)$ (keV)	K^π	J^π	$\frac{I_\gamma(\Delta I=2)}{I_\gamma(\Delta I=1)}$	gk-gr	δ
^{181}Re	191.6	355.8	$9/2^-$	$13/2^-$	0.139(2)	0.942(48)	0.21(1)
	215.3	406.9	$9/2^-$	$15/2^-$	0.286(82)	0.98(10)	0.19(2)
	238.3	453.5	$9/2^-$	$17/2^-$	0.435(151)	0.99(13)	0.18(2)
	255.5	493.7	$9/2^-$	$19/2^-$	0.667(222)	0.95(12)	0.18(2)
	273.9	529.1	$9/2^-$	$21/2^-$	0.714(204)	1.03(11)	0.17(2)
	281.9	555.6	$9/2^-$	$23/2^-$	0.833(139)	1.063(64)	0.15(1)
	294.7	576.2	$9/2^-$	$25/2^-$	0.909(248)	1.07(11)	0.14(1)
^{183}Re	197.0	364.8	$9/2^-$	$13/2^-$	0.125(11)	0.943(30)	0.20(1)
	223.6	420.7	$9/2^-$	$15/2^-$	0.339(27)	0.852(25)	0.21(1)
	250.3	473.9	$9/2^-$	$17/2^-$	0.426(41)	0.968(34)	0.19(1)
	273.2	523.5	$9/2^-$	$19/2^-$	0.610(55)	0.969(32)	0.18(1)
	298.6	571.7	$9/2^-$	$21/2^-$	0.802(88)	0.960(38)	0.18(1)
	315.0	613.4	$9/2^-$	$23/2^-$	1.16(15)	0.902(43)	0.18(1)
	342.1	656.7	$9/2^-$	$25/2^-$	1.25(20)	0.931(+50/-59)	0.18(1)
	350.3	692.4	$9/2^-$	$27/2^-$	1.20(23)	1.068(+67/-82)	0.15(1)
	360.9	711.1	$9/2^-$	$29/2^-$	1.72(46)	0.92(+ 8/-10)	0.16(2)
	407.0	766.5	$9/2^-$	$31/2^-$	2.9(11)	0.71(+ 8/-13)	0.22(3)
^{185}Re	210.7	389.1	$9/2^-$	$13/2^-$	7.5 (37)	0.971(52)	0.20(1)
	237.5	448.2	$9/2^-$	$15/2^-$	3.3 (16)	0.972(0)	0.20(0)
	308.3	588.8	$19/2^-$	$17/2^-$	1.5 (02)	0.198(24)	0.82(10)

Table 4.2: Calculated $|g_K - g_R|$ values and mixing ratios δ, for $\Delta J = 1$ transitions in the $K = 9/2^-$ band for odd mass rhenium isotopes with mass numbers 181, 183, and 185. The quadrupole moment (Q_0) used for ^{181}Re was 7.5 eb and for ^{183}Re and ^{185}Re, the values used were 6.5 eb. The $K = 19/2^-$ band for ^{185}Re is also included for a later comparison with theoretical predictions

to have a configuration of $\nu\{3/2^-[512], 11/2^+[615]\} \otimes \pi 5/2^+[402]$.

4.3 Multi-quasiparticle Calculations

The level scheme for ^{185}Re shown in Figure 3.2 has been deduced almost exclusively by experimental techniques other than consideration of the hindered decays from the 1207 keV state. Excited intrinsic states at 1109 keV ($13/2^-$), 1207 keV ($15/2^-$), 1380 keV ($17/2^-$), 1411 keV ($19/2^-$), 2009 keV ($23/2^-$) and 2124 keV ($25/2^-$) are clearly identified. To assign configurations, we have performed multi-quasiparticle calculations to calculate the energies of the different possible configurations. This is achieved by calculating single-particle energies for the intrinsic states in the Nilsson model, transforming to quasiparticle energies, including self-consistent pairing using the Lipkin-Nogami model and summing the resultant energies for each configuration [42, 31]. The resulting calculation will be different depending on the nucleon configuration and the deformation of the individual nuclei. Assuming a deformation parameter of $\epsilon_2 = 0.217$ and $\epsilon_4 = 0.093$ for ^{185}Re [14], the energies of the intrinsic states were calculated by Dr. Greg Lane from the Department of Nuclear Physics. These calculated excitation energies are presented in graphical form in Figure 4.1.

The calculated energy for the lowest state with a spin and parity $25/2^+$ is 2216 keV,

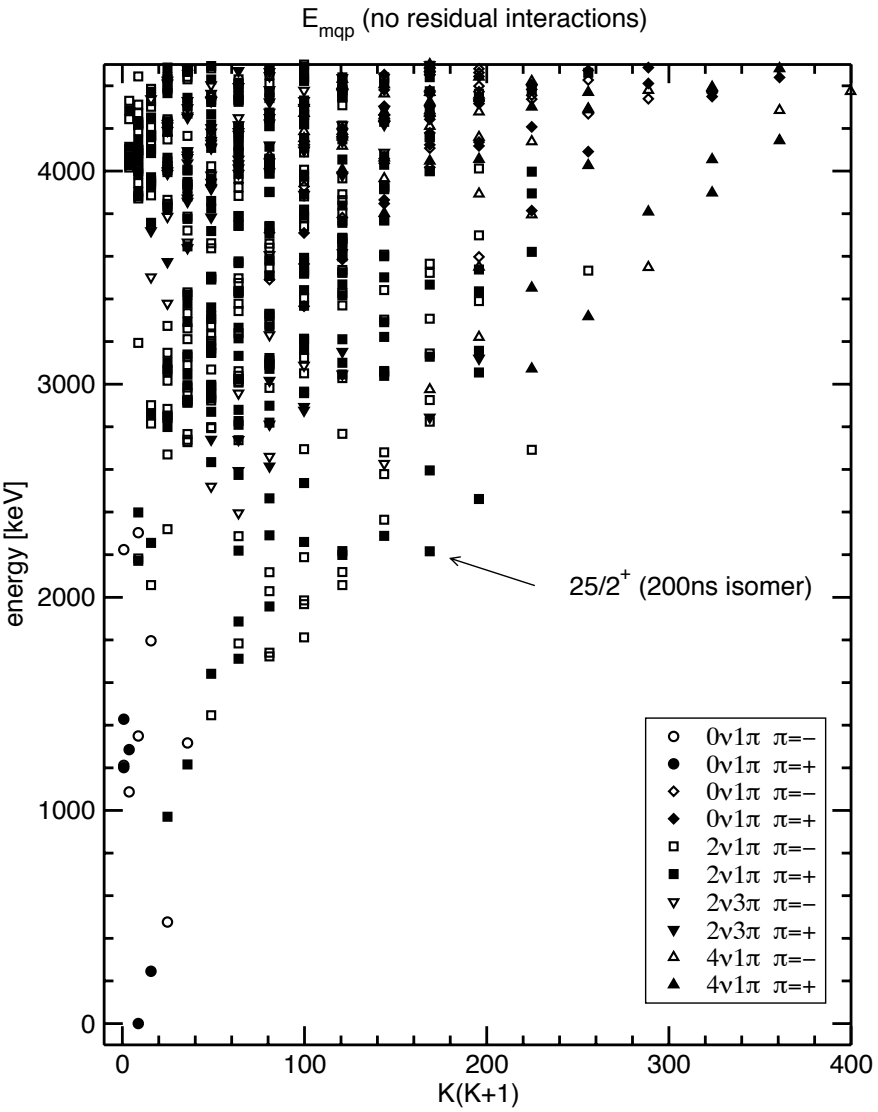

Figure 4.1: Single-particle energies in the y-axis for intrinsic states with spin K calculated for ^{185}Re with $K(K+1)$ in the x-axis. The filled and hollow symbols represent positive and negative parity respectively. The single-particle states shown are states with one, three and five particles denoted by $0\nu1\pi$ (one proton), $2\nu1\pi$ (two neutrons, one proton), $2\nu3\pi$ (two neutrons, three protons), and $4\nu1\pi$ (four neutrons, one proton)

in good agreement with 2124 keV measured for the 200 ns isomer in ^{185}Re, also with the same spin and parity. Figure 4.1 shows that the $K^\pi = 25/2^+$ state can only decay by M2 or E3 transitions into other intrinsic states. However, the $25/2^+$ isomer was observed (see Figure 3.2) to decay to a state with a spin and parity of $23/2^-$. This experimental observation is not, however, inconsistent with theory, because the calculation in Figure 4.1 ignores the residual interactions between particular single particles in configurations involving more than one nucleon. The residual interaction for the single particles which make up the three-particle configurations of ^{185}Re can be calculated from simple two-particle

states measured for nuclei with odd numbers of protons and neutrons [43, 44]. They are presented in Table 4.3 for different single-particle configurations in ^{185}Re. The energies from the graph in Figure 4.1(E_{mqp}) are added to the residual interactions (E_{res}) to obtain the true calculated energies (E_{calc}) for the multi-particle configurations, and compared with experimental observations (E_{expt}).

K^π	Configuration	E_{mqp} (keV)	E_{res} (keV)	E_{calc} (keV)	E_{expt} (keV)	ΔE
$25/2^+$	$\nu\{9/2^+[624], 11/2^+[615]\} \otimes \pi 5/2^+[402]$	2216	-28	2188	2124	+64
$23/2^-$	$\nu\{9/2^+[624], 7/2^-[503]\} \otimes \pi 7/2^+[404]$	2364	-311	2053	2009	+44
$19/2^-$	$\nu\{3/2^-[512], 11/2^+[615]\} \otimes \pi 5/2^+[402]$	1812	-197	1615	1411	+204
$17/2^-$	$\nu\{9/2^+[624], 3/2^-[512]\} \otimes \pi 5/2^+[402]$	1723	-176	1547	1380*	+167
	$\nu\{11/2^+[615], 1/2^-[510]\} \otimes \pi 5/2^+[402]$	1710	-30	1740	1380*	+330
$15/2^-$	$\nu\{9/2^+[624], 1/2^-[510]\} \otimes \pi 5/2^+[402]$	1784	-9	1775	1207*	+568
	$\nu\{11/2^-[615], 1/2^-[510]\} \otimes \pi 5/2^+[402]$	1740	-29	1711	1207*	+504
$13/2^-$	$\nu\{3/2^-[512], 1/2^-[510]\} \otimes \pi 9/2^+[514]$	1447	-145	1302	1109	+193
$9/2^-$	$\pi 9/2^-[514]$	476	n/a	476	368	+108
$5/2^+$	$\pi 5/2^+[402]$	0	n/a	0	0	0

Table 4.3: The energies for various single-particle configurations in ^{185}Re. The theoretical value is corrected for residual interactions, and the difference between the theoretical calculations and experimental observations is denoted by ΔE. *Note that there are two possibilities suggested for each of the 1207 and 1380 keV experimental states.

The $23/2^-$ state has a large residual interaction energy (E_{res}) and drops down 311 keV in the y-axis of Figure 4.1 to lie below the $25/2^+$ isomer. This implies that the $25/2^+$ isomer can decay directly to the $23/2^-$ state, agreeing with experimental observation. Furthermore, the calculated energies for the $25/2^+$ and the $23/2^-$ states agree very well with experimental measurements (within 100 keV). However, the calculated energies for the $17/2^-$, $15/2^-$ and the $13/2^-$ states deviate from experimental measurements by large amounts, up to ~ 600 keV.

The discrepancies may be explained by an observation performed on a neighbouring nucleus, ^{184}W, which has the same number of neutrons. There is an especially favoured 5^- state in ^{184}W which lies at 1285 keV, which is due to the $\nu 11/2^-[615] \otimes \pi 1/2^-[510]$ configuration [45]. One of the possible configurations for the $15/2^-$ state in ^{185}Re is just this state added to the $5/2^+[402]$ ground state (with zero energy). Therefore, based on the $\nu 11/2^-[615] \otimes \pi 1/2^-[510]$ configuration in ^{184}W, we would predict a $15/2^-$ state in ^{185}Re at $1285 - 28 = 1257$ keV, where 28 keV is the energy due to residual interactions. This is close to the experimental value of 1207 keV, and radically different from the present calculation of 1711 keV. So, it is clear from the ^{184}W neighbour that a spin and parity assignment of $15/2^-$ to the 1207 keV level is reasonable.

Also, both the states with spins $17/2^-$ and $15/2^-$ involve a particle in the $1/2^-[510]$ Nilsson state. This particle is also present in the 5^- state in ^{184}W mentioned previously. There could be a problem with the residual interaction calculation for that single-particle state, since the higher $23/2^-$ and $25/2^-$ states where the calculated energies agree with experimental measurements, do not involve the $1/2^-[510]$ particle. If the single-particle energy for the $1/2^-[510]$ particle turns out to be lower in magnitude than the present calculation, the favoured configuration for the $17/2^-$ state might be $\nu 11/2^+[615], 1/2^-[510] \otimes \pi 5/2^+[402]$ (see Table 4.3), where the calculated energy, E_{calc} is

expected to drop by $\sim$ 500 keV. Nevertheless, the theoretical calculations for the $1/2^{-}[510]$ particle would need to be investigated further before making any firm conclusions. However, it is beyond the scope of the current work.

Conclusions

High spin states in ^{185}Re were populated in inelastic collisions between an enriched ^{185}Re target and 820 MeV ^{136}Xe ions. The emitted γ-rays were observed with Gammasphere and a new level scheme for ^{185}Re was constructed.

The states which are fed by the isomer at 2124 keV in ^{185}Re were investigated extensively. The techniques of γ-ray coincidence analysis were used, and new transitions at 98, 173, 562, 659, 741 and 124 keV unobserved previously were found together with three new intrinsic states, hence extending the level scheme below the 2124 keV isomer. The level structure above this isomer was also investigated, and new γ-rays with energies of 88, 351, 394 and 605 keV were discovered. However, further investigation on the spins, parities, and the nature of the states above the 2124 keV level could not be performed due to time constraints.

However, the states fed by the 2124 keV isomer were thoroughly investigated. The spins and parities of the states from the 1109 keV level to the 2124 keV level were determined by angular corelations between the transitions below the 2124 keV level. The 1109 keV level was assigned as $13/2^-$. The 1411 keV level is an intrinsic state with a rotational band observed up to 2000 keV. The spin and parity of this level was assigned as $19/2^-$, with $21/2^-$ and $23/2^-$ at 1692 keV and 2000 keV respectively for the rotational band. The intrinsic state at 2009 keV was assigned as $23/2^-$, the same as the 2000 keV level. The order of the 31 keV transition and the 173 keV transition could not be determined. Since the 31 keV transition is very low in energy, it was assumed to depopulate the 1411 keV isomer, and a new intrinsic state was placed tentatively at 1380 keV with a spin assignment of $17/2^-$. There is an ambiguity in assigning a spin and parity for the 1207 keV level from angular correlations, so the reduced hindrances, f_ν of the transitions depopulating the 1207 keV level were calculated, and the spin and parity assignment of $15/2^-$ which gives $f_\nu \sim 100$ was selected for the 1207 keV level.

The mixing ratios for the mixed M1/E2 transitions in the $K^- = 9/2^-$ band was measured as ~ 0.2 from both the angular correlations and the $\Delta J = 2/\Delta J = 1$ branching ratios, in good agreement with the $K^- = 9/2^-$ bands which are also present in other odd-mass rhenium isotopes, ^{181}Re and ^{183}Re. The rotational band with $K^\pi = 19/2^-$ in ^{181}Re was measured to have a mixing ratio of ~ 0.7 for the $\Delta J = 1$ transitions, again from both the angular correlations and the $(\Delta J = 2)/(\Delta J = 1)$ branching ratios.

The single-particle configurations for the new intrinsic states were also deduced and compared with experimental predictions based on multi-quasiparticle calculations of the expected intrinsic state energies. The configurations for the $13/2^-$, $15/2^-$, $19/2^-$, $23/2^-$ and $25/2^-$ were confidently assigned as $\nu\{3/2^-[512], 1/2^-[510]\} \otimes \pi 9/2^+[514]$, $\nu\{9/2^+[624], 1/2^-[510]\} \otimes \pi 5/2^+[402]$, $\nu\{3/2^-[512], 11/2^+[615]\} \otimes \pi 5/2^+[402]$, $\nu\{9/2^+[624], 7/2^-[503]\} \otimes \pi 7/2^+[404]$, $\nu\{9/2^+[624], 11/2^+[615]\} \otimes \pi 5/2^+[402]$ respectively.

Future work should focus on understanding the discrepancies for states involving the $1/2^-[510]$ orbital and identifying the structure above the $T_{1/2} = 200$ ns isomer.

Bibliography

[1] K. S. Krane, *Introductory Nuclear Physics*, (New York, 1988)

[2] N. A. Jelley, *Fundamentals of Nuclear Physics*, (Cambridge University Press, 1990)

[3] R. F. Casten, *Nuclear Structure from a Simple Perspective*, (Oxford University Press, 1990)

[4] H. Ejiri and M. J. A. de Voight, *Gamma-ray and Electron Spectroscopy in Nuclear Physics*, (Oxford, 1989)

[5] A. Bohr and B. R. Mottelson, *Nuclear Structure*, **Volume II**, (London 1975)

[6] V. F. Weisskopf, Phys. Rev. **83**, 1073 (1951)

[7] K. M. Alder and R. M. Steffen, *The Electromagnetic Interaction in Nuclear Spectroscopy*, Chapter 2, edited by W. D. Hamilton (North-Holland 1975)

[8] K. E. B. Löbner, *The Electromagnetic Interaction in Nuclear Spectroscopy*, Chapter 5, edited by W. D. Hamilton (North-Holland 1975)

[9] National Nuclear Data Center, *Brookhaven National Laboratory*, (www.nndc.bnl.gov)

[10] A. Bohr and B. R. Mottelson, *Nuclear Structure*, **Volume I**, (London 1975)

[11] K. E. G. Löbner, Phys. Lett. B **26**, 369 (1968)

[12] A. B. Hayes *et.al.*, Phys. Rev. Lett., **89** 24 (2002)

[13] C. S. Purry *et. al.*, Nucl. Phys. A **632** 229 (1988)

[14] W. Nazarewicz, M. A. Riley and J. D. Garrett, Nucl. Phys. A **512**, 61-96 (1990)

[15] T. Shizuma *et.al.*, Z. Phys. A **359**, 229-230 (1997)

[16] A. P. Byrne, *Inclusion of a Prompt Resolution Function into Lifetime Curves*, ANU-P/957, The Australian National University (1986)

[17] A. R. Poletti *et. al.*, Phys. Rev. C **13**, 1180-1193 (1976)

[18] R. Broda *et. al.*, Phys. Rev. C **49**, R575-R579 (1994)

[19] M. W. Drigert, J. A. Cizewski, M. S. Rosenthal and A. W. Wright, Phys. Rev. C **32** 136-144 (1985)

[20] C. W. Beausang *et. al.*, Nucl. Instrum. Methods A **313** 37 (1992)

[21] F. A. Beck *et. al.*, Proc. Workshop Large Gamma-ray Detector Arrays, Chalk River, Canada AECL **10613**, 364 (1992)

[22] P. J. Nolan, F. A. Beck, D. B. Fossan, Annu. Rev. Nucl. Part. Sci., **45**, 561-607 (1994)

[23] Department of Physics, *University of Jyväskylä*, World Wide Web (www.phys.jyu.fi/research/gamma/publications/ptgthesis/node35.html

[24] F. Rösel, H. M. Fries, K. Alder and H. C. Pauli, At. Data Nucl. Data Tables **21** 29 (1978)

[25] E. S. Paul, *Angular correlation analysis with EUROGRAM II*, Oliver Lodge Laboratory, University of Liverpool, (September 1995)

[26] K. S. Krane, R. M. Steffen, and R. M. Wheeler, Nucl. Data Tables **A11**, 351 (1973)

[27] L. P. Ekström and A. Nordlund, Nucl. Instrum. and Methods **A313**, 421 (1992)

[28] G. D. Dracoulis *et. al.*, Physics Letters B **584** 22-30 (2004)

[29] G. D. Dracoulis *et. al.*, Phys. Rev. C **71**, 044326 (2005)

[30] G. D. Dracoulis *et. al.*, Physics Letters B **635**, 200-206 (2006)

[31] F. G. Kondev *et. al.*, Nucl. Phys. A **617**, 91-130 (1997)

[32] T. Kibédi, T. W. Burrows, M. B. Trzaskovskaya, C. W. Nestor Jr, *BRICC Program Package v 2.0*, (29 September 2005)

[33] D. C. Radford, Nucl. Instrum. Methods, A **361**, 297-305 (1995)

[34] M. Cromaz *et. al.*, Nucl. Instrum. Methods A **462** 519-529 (2001)

[35] J. Aron *et.al.*, Rev. Sci. Instrum., **57** 739 (1986)

[36] P. J. Daly *et. al.*, Phys. Rev. C **59**, 6 (1999)

[37] M. Evans, A. E. Ellis, J. R. Leigh and J. O. Newton, Phys. Lett. B **34** 7, 609-611 (1971)

[38] G. J. Lane, *Coexistence and Structure of Deformed Shapes Near the $Z = 82$ Closed Shell*, PhD Thesis, The Australian National University (1995)

[39] C. J. Pearson *et. al.*, Nucl. Phys. A **674**, 301-329 (2000)

[40] C. S. Purry *et. al.*, Nucl. Phys. A **672**, 54-88 (2000)

[41] At. Dt. and Nucl. Data Tables, **42**, 189-291 (1989)

[42] Kiran Jain *et. al.*, Nucl. Phys. A **591**, 61-84 (1995)

[43] C. J. Gallagher Jr. and S. A. Moszkowski, Phys. Rev. **111** 1282-1290 (1958)

[44] C. J. Gallagher Jr., Phys. Rev. **126**, 1525-1531 (1962)

[45] C. Wheldon *et. al.*, Eur. Phys. J. A **20**, 365-369 (2004)